

Vertically stratified two-phase flow in a curved channel: Insights from a domain perturbation analysis

P. Garg, J. R. Picardo, and S. Pushpavanam

Citation: *Physics of Fluids* (1994-present) **26**, 073604 (2014); doi: 10.1063/1.4889738

View online: <http://dx.doi.org/10.1063/1.4889738>

View Table of Contents: <http://scitation.aip.org/content/aip/journal/pof2/26/7?ver=pdfcov>

Published by the [AIP Publishing](#)

Articles you may be interested in

[The impact of deformable interfaces and Poiseuille flow on the thermocapillary instability of three immiscible phases confined in a channel](#)

Phys. Fluids **25**, 024104 (2013); 10.1063/1.4790878

[Noncoincidence of separatrices in two-layer modons](#)

Phys. Fluids **19**, 056602 (2007); 10.1063/1.2731741

[Plane Poiseuille flow of a sedimenting suspension of Brownian hard-sphere particles: Hydrodynamic stability and direct numerical simulations](#)

Phys. Fluids **18**, 054103 (2006); 10.1063/1.2199493

[Mechanisms for deposition and resuspension of heavy particles in turbulent flow over wavy interfaces](#)

Phys. Fluids **18**, 025102 (2006); 10.1063/1.2166453

[The onset of gas pull-through during dual discharge from a stratified two-phase region: Theoretical analysis](#)

Phys. Fluids **16**, 3385 (2004); 10.1063/1.1771619



2014 Special Topics

PEROVSKITES | 2D MATERIALS | MESOPOROUS MATERIALS | BIOMATERIALS/ BIOELECTRONICS | METAL-ORGANIC FRAMEWORK MATERIALS

AIP | APL Materials

Submit Today!

Vertically stratified two-phase flow in a curved channel: Insights from a domain perturbation analysis

P. Garg,¹ J. R. Picardo,² and S. Pushpavanam^{2,a)}

¹Department of Chemical Engineering, Indian Institute of Technology Roorkee, Roorkee 247 667, India

²Department of Chemical Engineering, Indian Institute of Technology Madras, Chennai 600 036, India

(Received 12 February 2014; accepted 27 June 2014; published online 17 July 2014)

In this work, we investigate the fully developed flow field of two vertically stratified fluids (one phase flowing above the other) in a curved channel of rectangular cross section. The domain perturbation technique is applied to obtain an analytical solution in the asymptotic limit of low Reynolds numbers and small curvature ratios (the ratio of the width of the channel to its radius of curvature). The accuracy of this solution is verified by comparison with numerical simulations of the nonlinear equations. The flow is characterized by helical vortices within each fluid, which are driven by centrifugal forces. The number of vortices and their direction of circulation varies with the parameters of the system (the volume fraction, viscosity ratio, and Reynolds numbers). We identify *nine* distinct flow patterns and organize the parameter space into corresponding flow regimes. We show that the fully developed interface between the fluids is not horizontal, in general, but is deformed by normal stresses associated with the circulatory flow. The results are especially significant for flows in microchannels, where the Reynolds numbers are small. The mathematical results in this paper include an analytical solution to two coupled biharmonic partial differential equations; these equations arise in two-phase, two-dimensional Stokes flows. © 2014 AIP Publishing LLC. [<http://dx.doi.org/10.1063/1.4889738>]

I. INTRODUCTION

In this work, we study the fully developed flow of two vertically stratified immiscible fluids in a curved channel. The channel has a rectangular cross section and is curved along the streamwise direction. We focus on the regime of low Reynolds numbers (Re). However, this is not a Stokes flow problem (i.e., $Re \neq 0$). The centrifugal force has a significant qualitative impact on the flow field at non-zero (though small) Reynolds numbers – it generates helical vortices. This circulatory motion, in turn, affects the balance of normal forces at the interface. Thus, the shape of the interface cannot be specified *a priori*. In this analysis, we study these features of the two-phase flow by deriving an asymptotic solution for small Reynolds numbers and a gently curved channel. This solution is used to gain physical insight into the hydrodynamic phenomena and to understand the effects of different fluid properties and operating conditions on the flow field.

Fluid flowing in a curved channel experiences a centrifugal force that drives a secondary circulatory flow. In the case of a single fluid, two counter-rotating helical vortices are formed as reported first by Dean;¹ these vortices are now called Dean vortices. While Dean studied channels with a circular cross section, Cuming² extended his work to channels with elliptic and rectangular cross-sections. These early studies analyzed regular perturbation solutions for channels of small dimension and gentle curvature, to gain insight into the key features of the flow at low Reynolds

^{a)} Author to whom correspondence should be addressed. Electronic mail: spush@iitm.ac.in. Tel.: +91-44-2254161. Fax: +91-44-22570509.

numbers. Subsequently, several numerical studies have investigated the flow at high Reynolds numbers, in sharply curved channels; these have been reviewed in detail by Berger *et al.*³ Work has also been done on the instability and bifurcation of the primary Dean vortex flow.^{4,5}

In contrast, only a few theoretical studies have been carried out, thus far, on two-phase flows in curved channels. Advances in computational power have now made it possible to study these flows numerically. Recent computational work has been done on the core-annular flow regime⁶ and the slug flow regime.^{7,8} Vertically stratified flow – the problem addressed in this work – has been studied via finite volume simulations by Gelfgat *et al.*⁹ They investigated the effect of increasing the Reynolds numbers and the channel curvature on the cross flow. However, only a limited range of parameter values were investigated; thus, only one flow pattern was found. A complementary study, which analyzes the system across parameter space, is required to unveil the full range of hydrodynamic behavior.

The qualitative nature of the axial velocity profile in two-phase flow, and the interaction between the two fluids, is strongly dependent on the parameters. Thus, a variety of flow patterns are found in two-phase flow when the full range of parameter values are considered. The strength of the centrifugal force experienced by the fluids depends on the magnitude of the axial velocity. For the single-phase case, the maximum of the axial velocity, and thus the maximum of the centrifugal force, always lies at the center of the channel. Hence the fluid at the center is forced outwards, strongly, in the direction of the centrifugal force; this fluid then recirculates along the top and bottom walls, setting up two counter-rotating vortices. For vertically stratified two-phase flow, when the maxima lies near the interface, the flow field is similar to that of single-phase flow; two vortices are formed – one in each fluid. However, on varying the parameters, the maxima of the axial velocity can move into the bulk of either fluid. If the maxima is present in the top fluid, then we anticipate the presence of 2 vortices within the top fluid itself, and at least one in the bottom fluid.

Apart from the influence of the axial velocity profile, the interaction between the vortices at the interface is expected to generate more patterns. This inter-fluid interaction is responsible for a range of flow patterns in *core-annular* flow in a curved circular channel – recently studied by Picardo and Pushpavanam,¹⁰ using an asymptotic solution at low Reynolds numbers. They identified five different flow patterns; we expect a similar variety of circulation patterns when the fluids are vertically stratified.

Another feature of interest is the behavior of the interface in the presence of normal stresses. These stresses are exerted by the two fluids on either side of the interface. The magnitude of the normal stress depends on the strength of the circulatory flow within each fluid. While these forces tend to deform the interface, surface tension attempts to keep it flat. Thus the fully developed configuration of the interface results from a balance between capillary forces and flow forces – both viscous and centrifugal.

There has been a sustained interest in analyzing flow in curved channels due to their wide applicability. The secondary flow leads to improved heat and mass transfer coefficients as well as enhanced mixing.³ This makes curved channels especially useful for industrial applications.¹¹ Curved channels are also widely prevalent in nature. For instance blood vessels in humans, especially the aorta, are highly curved.¹² Recent advances in microfluidics have brought curved microchannels into focus because of their ability to substantially enhance mixing in the low Reynolds number regime.^{13,14} Stable vertically stratified two-phase flows have been observed recently in microchannels, where Reynolds numbers are low and capillary forces dominate gravity.^{15,16} Kuban *et al.*¹⁶ have experimentally observed stable vertically stratified flow in a straight microchannel for Reynolds numbers ranging from 10 to 80. (Here, Re is defined on the basis of the pressure gradient, as given in Sec. II.) These flows have applications in solvent extraction^{16–18} and phase transfer catalysis.¹⁹ Here, a solute is transferred across the interface from one fluid stream to the other. The additional mixing in curved microchannels will enhance the performance of these devices.¹⁰

With the aim of elucidating the underlying physical mechanisms, we address the problem of vertically stratified flow in the limit of a gently curved channel and low Reynolds numbers. We apply the method of domain perturbations,²⁰ which approximates the solution of the velocity field and interface location as a small deviation from their straight channel counterparts. We also assume a 90° contact angle between the interface and the walls; this simplifies the analysis and permits

an analytical solution. This solution enables us to carry out detailed parametric studies, at a low computational cost, to unravel features of the flow which would otherwise be missed. Our objective is to identify all possible flow patterns in a systematic manner, to analyze the nature and extent of interface deformation, and to identify general principles which will aid in the design of curved microchannels for specific pairs of fluids. Once the flow regimes are identified, targeted numerical simulations are performed to check the accuracy of the perturbation solution at finite Reynolds numbers and curvature ratios.

This problem is characterized by four macroscopic quantities: the axial pressure drop, the holdup or volume fraction (which is defined as the fraction of the total channel's volume occupied by the top fluid), and the flow rates of each fluid. To specify the problem completely, we must provide the value of any two of these flow quantities as inputs. (A similar situation holds true for stratified flow in straight channels.²¹) In this work, we choose to specify the holdup (which determines the interface position) and the pressure drop. These inputs must then be satisfied by the perturbation solution at all orders of the curvature ratio. The flow rates may then be calculated after obtaining the solution. In case the flow rates are specified as inputs, the solution must be determined iteratively, beginning with an initial guess for the pressure drop and holdup.

The paper is organized in the following manner. In Sec. II, the governing equations and boundary conditions are presented. In Sec. III, we derive the asymptotic solution using the domain perturbation method.²⁰ This calculation involves solving two coupled biharmonic equations analytically, for which we extend the method of superposition to two-phase problems (it has been used previously in single phase flow²²). The technique is detailed in the Appendix. We begin the analysis of the flow field in Sec. IV; we discuss nine qualitatively different flow patterns, along with visualizations of the flow field. In Sec. V, we analyze the effect of parameters in detail. We present a simple method to compute flow regime maps, which are used to understand the physical mechanisms underlying the multiplicity of flow patterns. With potential applications in mind, we briefly study the dependence of the strength of the cross flow on the aspect ratio of the channel in Sec. VI. In Sec. VII, we describe the effect of the cross-flow on the shape of the interface. The generic features of the deformed interface are identified here, and their quantitative dependence on the parameters is studied. The perturbation solution is compared with numerical simulations of the nonlinear equations in Sec. VIII. We end by summarizing the key results and discussing their significance in Sec. IX.

II. GOVERNING EQUATIONS

The flow configuration under study consists of two, vertically stratified, immiscible fluids, flowing through a gently curved channel. A schematic of the system, with the curvilinear coordinate system (x, y, θ) , is depicted in Fig. 1. The origin of the x - y plane (O') is located at the center of a cross section of the channel. The azimuthal θ coordinate determines the axial position of this cross section. The fluid located in the lower part of the channel is labeled as fluid 1, while the one

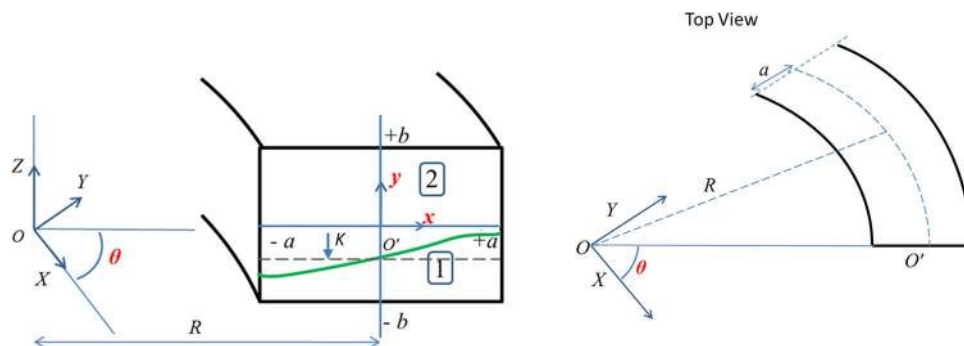


FIG. 1. Cross sectional view and top-view of vertically stratified flow in a curved channel. The (X, Y, Z) axes represent the Cartesian co-ordinate system, while (x, y, θ) axes represent the curvilinear co-ordinate system used in this paper. The dashed line, located at K , marks the position that the interface would have if the channel were straight.

above is called fluid 2. The width (x -direction) and height (y -direction) of the channel are $2a$ and $2b$, respectively. The position of the interface, which is unknown *a priori*, is represented by a curve, that is displaced from a horizontal dashed line. This dashed line, located at K , marks the position that the interface would have if the channel were straight.

The flow field is assumed to be fully developed and driven by a constant pressure drop $\frac{\partial P}{\partial \theta}$ in the axial direction. The characteristic scales used to define the non-dimensional variables are

$$x_c = a, \quad y_c = b, \quad V_{c,i} = \frac{-(\Delta P)a^2}{\mu_i}, \quad P_c = -(\Delta P)a$$

with $\Delta P = -\frac{1}{R} \frac{\partial P}{\partial \theta}$.

Here, ΔP is the magnitude of the azimuthal pressure gradient, along the centerline of the channel (located at radial distance R from the point O in Fig. 1). The pressure and velocity scales are chosen to reflect the balance between the axial pressure gradient and the viscous forces, as is characteristic of Poiseuille flow at low Reynolds numbers.

The dimensional and non-dimensional variables (denoted by a prime) are related in the following manner:

$$x = x_c x', \quad y = y_c y', \quad P_i = P_c P'_i, \quad (u_i, v_i, w_i) = V_c (u'_i, v'_i, w'_i),$$

where i ($= 1, 2$) is an index which denotes the fluid.

This choice of scales leads to the following non-dimensional groups:

$$\lambda = \frac{a}{b}, \quad \varepsilon = \frac{a}{R}, \quad k = \frac{K}{b}, \quad \mu_{12} = \frac{\mu_1}{\mu_2}, \quad Re_i = \frac{\rho_i (\Delta P) a^3}{\mu_i^2}, \quad Ca = \frac{(\Delta P) a^2}{\gamma}.$$

Here λ is the aspect ratio of the channel (ratio of width to height), ε is the curvature ratio of the channel, μ_{12} is the viscosity ratio of the two fluids, Re_i is the Reynolds number of each fluid, Ca is the capillary number (γ is the surface tension of the interface), and k is the non-dimensional position that the interface would have in a straight channel. This position is directly determined by specifying the holdup or volume fraction of fluid 2, α (the ratio of the volume of phase 2 to the volume of the channel), i.e., $\alpha = (1 - k)/2$. The pressure drop (ΔP) and the holdup (α) are inputs, which are required to uniquely specify the problem.

Since the density ratio only affects the relative inertial forces in the momentum equation, we do not define it as an independent parameter. Instead the effects of the fluid densities are captured by Re_1 and Re_2 . On the other hand, the viscosity ratio has an independent effect in the balance of viscous tangential stresses at the inter-fluid interface, which is not captured by the Reynolds numbers. Hence, the viscosity ratio appears as a separate parameter in the equations. Scaling the equations in this manner facilitates a clear understanding of the underlying physics.

The equations governing the system are the continuity equation and the Navier-Stokes equations. After simplifying these equations for the case of fully developed flow, and rewriting in terms of the aforementioned dimensionless variables (the prime is dropped for convenience), we obtain

$$\frac{\partial u_i}{\partial x} + \lambda \frac{\partial v_i}{\partial y} + \varepsilon \frac{u_i}{(1 + x\varepsilon)} = 0, \quad (1)$$

$$Re_i \left[u_i \frac{\partial u_i}{\partial x} + \lambda v_i \frac{\partial u_i}{\partial y} - \varepsilon \frac{w_i^2}{(1 + x\varepsilon)} \right] = \frac{\partial P_i}{\partial x} + \lambda^2 \frac{\partial^2 u_i}{\partial y^2} - \lambda \frac{\partial^2 v_i}{\partial x \partial y}, \quad (2)$$

$$Re_i \left[u_i \frac{\partial v_i}{\partial x} + \lambda v_i \frac{\partial v_i}{\partial y} \right] = -\lambda \frac{\partial P_i}{\partial y} + \frac{\partial^2 v_i}{\partial x^2} - \lambda \frac{\partial^2 u_i}{\partial y \partial x} + \frac{\varepsilon}{(1 + x\varepsilon)} \left(\frac{\partial v_i}{\partial x} - \lambda \frac{\partial u_i}{\partial y} \right), \quad (3)$$

$$Re_i \left[u_i \frac{\partial w_i}{\partial x} + \lambda v_i \frac{\partial w_i}{\partial y} + \varepsilon \frac{w_i u_i}{(1 + x\varepsilon)} \right] = \frac{1}{(1 + x\varepsilon)} + \frac{\partial^2 w_i}{\partial x^2} + \lambda^2 \frac{\partial^2 w_i}{\partial y^2} + \frac{\varepsilon}{(1 + x\varepsilon)} \frac{\partial w_i}{\partial x} - \varepsilon^2 \frac{w_i}{(1 + x\varepsilon)^2}. \quad (4)$$

This form of the equations is obtained by substituting $\nabla^2 \bar{v} = -\nabla \times \nabla \times \bar{v} + \nabla(\nabla \cdot \bar{v})$ and applying the continuity equation for incompressible flow, $\nabla \cdot \bar{v} = 0$.

Along with Eqs. (1)–(4), we require 28 boundary conditions to uniquely specify the flow field. This includes 24 boundary conditions for the velocity field and 4 conditions for the position of the interface.

The no-slip condition at the wall yields the following 18 boundary conditions:

$$\{u_1, v_1, w_1\} = 0 \text{ at } y = -1 \text{ for } -1 \leq x \leq 1, \quad (5)$$

$$\{u_1, v_1, w_1\} = 0 \text{ at } x = \pm 1 \text{ for } -1 \leq y \leq F(x), \quad (6)$$

$$\{u_2, v_2, w_2\} = 0 \text{ at } y = +1 \text{ for } -1 \leq x \leq 1, \quad (7)$$

$$\{u_2, v_2, w_2\} = 0 \text{ at } x = \pm 1 \text{ for } F(x) \leq y \leq 1. \quad (8)$$

The location of the interface, in fully developed flow, may be represented explicitly as a function of x as follows:

$$y = F(x). \quad (9)$$

The unit normal vector to the interface is given by

$$\hat{n} = \left(\hat{e}_y - \frac{\partial F}{\partial x} \hat{e}_x \right) \left(1 + \left(\frac{\partial F}{\partial x} \right)^2 \right)^{-1/2}. \quad (10)$$

Requiring the velocity field to be continuous, at the interface, yields 3 boundary conditions

$$\{u_1, v_1, w_1\} = \mu_{12} \{u_2, v_2, w_2\} \text{ at } y = F(x) \text{ for } -1 \leq x \leq 1. \quad (11)$$

The kinematic condition must also be applied

$$v_1 - \frac{\partial F}{\partial x} u_1 = 0 \text{ at } y = F(x) \text{ for } -1 \leq x \leq 1. \quad (12)$$

The tangential stress balance at the interface gives 2 more boundary conditions

$$\hat{n} \cdot \bar{\sigma}_2 - (\hat{n} \cdot \hat{n} \cdot \bar{\sigma}_2) \hat{n} = \hat{n} \cdot \bar{\sigma}_1 - (\hat{n} \cdot \hat{n} \cdot \bar{\sigma}_1) \hat{n} \text{ at } y = F(x). \quad (13)$$

The normal stress balance yields

$$P_1 - P_2 + (\hat{n} \cdot \hat{n} \cdot \bar{\sigma}_2) - (\hat{n} \cdot \hat{n} \cdot \bar{\sigma}_1) = \frac{1}{Ca} \nabla \cdot \hat{n} \text{ at } y = F(x), \quad (14)$$

where $Ca = \frac{(\Delta P) a^2}{\gamma}$ is the Capillary number. It is the ratio of viscous forces to surface tension forces acting at the interface.

Three additional boundary conditions are needed to determine the shape of the interface. These are given by specifying the contact angle and the holdup/volume fraction of fluid 2.

Here, we assume the contact angle between the interface and the wall to be 90° for simplicity. This gives two conditions for the interface

$$\frac{dF(x)}{dx} = 0 \text{ at } x = \pm 1. \quad (15)$$

Finally, we require the interface to satisfy the input specification on the holdup (volume fraction) of fluid 2. This yields the last boundary condition

$$\frac{\int_{-1}^1 \int_{F(x)}^1 (1 + \varepsilon x) dy dx}{\int_{-1}^1 \int_{-1}^1 (1 + \varepsilon x) dy dx} = \alpha. \quad (16)$$

Note that the input pressure drop has been implicitly fixed by using it to define the velocity scale.

For a given channel geometry (i.e., fixed aspect ratio and curvature ratio), the parameters characterizing the system are viscosity ratio μ_{12} , holdup (α), Reynolds numbers (Re_1 and Re_2), and the capillary number (Ca).

III. SOLUTION BY DOMAIN PERTURBATION

The general solution of the nonlinear, governing Eqs. (1)–(4) is dependent on the curvature ratio ε . In the limit of a gently curved channel, i.e., a small curvature ratio ($\varepsilon \ll 1$), the perturbation approach²⁰ can be used to obtain an asymptotic analytical solution.

In this approach, the implicit dependence of the solution on ε is represented explicitly as a power series

$$u_i(x, y; \varepsilon) = u_{i,0}(x, y) + \varepsilon u_{i,1}(x, y) + \varepsilon^2 u_{i,2}(x, y) + O(\varepsilon^3), \quad (17)$$

$$v_i(x, y; \varepsilon) = v_{i,0}(x, y) + \varepsilon v_{i,1}(x, y) + \varepsilon^2 v_{i,2}(x, y) + O(\varepsilon^3), \quad (18)$$

$$w_i(x, y; \varepsilon) = w_{i,0}(x, y) + \varepsilon w_{i,1}(x, y) + \varepsilon^2 w_{i,2}(x, y) + O(\varepsilon^3), \quad (19)$$

$$P_i(x, y; \varepsilon) = P_{i,0}(x, y) + \varepsilon P_{i,1}(x, y) + \varepsilon^2 P_{i,2}(x, y) + O(\varepsilon^3), \quad (20)$$

$$F(x; \varepsilon) = k + \varepsilon f_1(x) + \varepsilon^2 f_2(x) + O(\varepsilon^3). \quad (21)$$

Here the first subscript denotes the fluid and the second subscript denotes the order of the term in the asymptotic expansion.

We substitute (17)–(21) into (1)–(16) and equate the coefficients of various powers of ε . This yields a series of linear problems, which must be solved sequentially to determine the coefficients in the asymptotic expansion. Applying the boundary conditions at the interface poses a problem, since the shape of the interface is not known *a priori*. To overcome this, a Taylor series expansion is used; it makes explicit, the implicit dependence of the solution on the shape of the interface. This procedure is called the *domain perturbation* method.²⁰ For instance, in the case of the continuity boundary condition (11) for u_i , we have

$$u_1 = \mu_{12} u_2 \quad \text{at } y = F(x)$$

$$u_1 + \varepsilon \left. \frac{\partial u_1}{\partial y} \frac{\partial F(x, \varepsilon)}{\partial \varepsilon} \right|_{\varepsilon=0} + O(\varepsilon^2) = \mu_{12} \left(u_2 + \varepsilon \left. \frac{\partial u_2}{\partial y} \frac{\partial F(x, \varepsilon)}{\partial \varepsilon} \right|_{\varepsilon=0} \right) + O(\varepsilon^2) \quad \text{at } y = k \quad (22)$$

On substituting Eqs. (17) and (21) into (22), we obtain

$$u_{1,0} + \varepsilon \left(u_{1,1} + \frac{\partial u_{1,0}}{\partial y} f_1 \right) + O(\varepsilon^2) = \mu_{12} \left(u_{2,0} + \varepsilon \left(u_{2,1} + \frac{\partial u_{2,0}}{\partial y} f_1 \right) \right) + O(\varepsilon^2) \quad \text{at } y = k. \quad (23a)$$

Equating the powers of ε yields the continuity conditions for $u_{i,0}$ and $u_{i,1}$,

$$u_{1,0} = \mu_{12}u_{2,0} \text{ at } y = k, \quad (23b)$$

$$\left(u_{1,1} + \frac{\partial u_{1,0}}{\partial y} f_1\right) = \mu_{12} \left(u_{2,1} + \frac{\partial u_{2,0}}{\partial y} f_1\right) \text{ at } y = k. \quad (23c)$$

In Subsections III A and III B, we calculate the solution up to $O(\varepsilon^1)$, which provides a good approximation for small curvature ratios and small Reynolds numbers. Moreover, it captures the key features of the flow field, i.e., the number of vortices, their direction of rotation, and the shape of the interface. The analytical solution is then analyzed over a wide range of parameter values to unravel the underlying physics.

A. Zeroth order solution

When $\varepsilon = 0$, the channel has no curvature. Hence, the zeroth order solution (ε^0) corresponds to the case of flow through a straight rectangular channel without any effects of curvature and centrifugal force. We refer to this as the base flow. Equating the coefficients of ε^0 from (2) to (4), we obtain the following equations:

$$u_{i,0} = 0, \quad (24)$$

$$v_{i,0} = 0, \quad (25)$$

$$\frac{\partial^2 w_{i,0}}{\partial x^2} + \lambda^2 \frac{\partial^2 w_{i,0}}{\partial y^2} = -1. \quad (26)$$

Thus, the flow is unidirectional and fully developed. The boundary conditions reduce to

$$w_{1,0} = 0 \text{ at } x = \pm 1 \text{ for } -1 \leq y \leq k, \quad (27)$$

$$w_{2,0} = 0 \text{ at } x = \pm 1 \text{ for } k \leq y \leq 1, \quad (28)$$

$$w_{1,0} = 0 \text{ at } y = -1 \text{ for } -1 \leq x \leq 1, \quad (29)$$

$$w_{2,0} = 0 \text{ at } y = 1 \text{ for } -1 \leq x \leq 1, \quad (30)$$

$$w_{1,0} = \mu_{12}w_{2,0} \text{ at } y = k \text{ for } -1 \leq x \leq 1, \quad (31)$$

$$\frac{\partial w_{1,0}}{\partial y} = \frac{\partial w_{2,0}}{\partial y} \text{ at } y = k \text{ for } -1 \leq x \leq 1. \quad (32)$$

The continuity equation (1), the normal stress boundary condition (13), and the conditions on the contact angle (15) are trivially satisfied. From (16) we have

$$\frac{1-k}{2} = \alpha, \quad (33a)$$

$$k = 1 - 2\alpha. \quad (33b)$$

Thus, the holdup is directly related to the interface position at $O(\varepsilon^0)$. In the analysis to follow, we study the flow field for different volume fractions (α), by varying k . This is more convenient as the latter appears directly in the equations.

The operator $\frac{\partial^2}{\partial x^2}$ in (26) is self-adjoint with homogenous boundary conditions (27) and (28); thus its eigen functions form a basis in $L_2[-1, 1]$ and can be used to represent the solution of (26). The general solution, based on this methodology, has been derived by Cornish:²³

$$w_{i,0} = \sum_{n=1}^{\infty} \frac{16(-1)^n}{\pi^3(2n+1)^3} \left(A_{i,n} \cosh \frac{(2n+1)\pi y}{2\lambda} + B_{i,n} \sinh \frac{(2n+1)\pi y}{2\lambda} + 1 \right) \left(\cos \frac{(2n+1)\pi x}{2} \right). \quad (34)$$

The integration constants $A_{1,n}$, $A_{2,n}$, $B_{1,n}$, and $B_{2,n}$ must be found by applying the boundary conditions (29)–(32). The series converges rapidly, and after 5 terms the incremental change is less than 0.1%. In fact, the first term captures all the important qualitative features of the flow, at $O(\varepsilon^0)$.

B. First order solution

The solution at $O(\varepsilon^1)$ takes into account the curvature of the channel and the effect of the resulting centrifugal force on the flow. Equating the coefficients of ε^1 from Eqs. (1) to (4), we obtain the following set of equations:

$$\frac{\partial u_{i,1}}{\partial x} + \lambda \frac{\partial v_{i,1}}{\partial y} = 0, \quad (35)$$

$$-\frac{\partial P_{i,1}}{\partial x} + \lambda^2 \frac{\partial^2 u_{i,1}}{\partial y^2} - \lambda \frac{\partial^2 v_{i,1}}{\partial y \partial x} = -\text{Re}_i w_{i,0}^2, \quad (36)$$

$$-\frac{\partial P_{i,1}}{\partial y} + \frac{\partial^2 v_{i,1}}{\partial x^2} - \lambda \frac{\partial^2 u_{i,1}}{\partial y \partial x} = 0, \quad (37)$$

$$\text{Re}_i \left(u_{i,1} \frac{\partial w_{i,0}}{\partial x} + \lambda v_{i,1} \frac{\partial w_{i,0}}{\partial y} \right) - \frac{\partial w_{i,0}}{\partial x} = \frac{\partial^2 w_{i,1}}{\partial x^2} + \lambda^2 \frac{\partial^2 w_{i,1}}{\partial y^2}. \quad (38)$$

In Eq. (36), the term $(-\text{Re}_i w_{i,0}^2)$ accounts for the effects of the centrifugal force. Thus the impact of the centrifugal force on a fluid at $O(\varepsilon^1)$ depends both on the base axial velocity ($w_{i,0}$) and the Reynolds number Re_i . For simplicity, only the first term of the expansion for $w_{i,0}$ is used in further analysis; all the major features of the flow are captured by it.

The first order axial velocity term ($w_{i,1}$) is absent from Eqs. (35) to (37). Hence, the secondary circulatory flow at $O(\varepsilon^1)$ is independent of $w_{i,1}$. The effect of $w_{i,1}$ will be observed only at $O(\varepsilon^2)$.

We determine the secondary flow in Subsection III B 1. We then study the deformation of the interface due to the secondary flow. Finally, the change in the flow rates, due to the modified axial velocity ($w_{i,1}$) and the deformation of the interface, is determined.

1. Calculation of the secondary flow field

The secondary flow field is governed by Eqs. (35)–(37), subject to the following boundary conditions:

$$\{u_{1,1}, v_{1,1}\} = 0 \text{ at } x = \pm 1 \text{ for } -1 \leq y \leq k, \quad (39)$$

$$\{u_{2,1}, v_{2,1}\} = 0 \text{ at } x = \pm 1 \text{ for } k \leq y \leq 1, \quad (40)$$

$$\{u_{1,1}, v_{1,1}\} = 0 \text{ at } y = -1 \text{ for } -1 \leq x \leq 1, \quad (41)$$

$$\{u_{2,1}, v_{2,1}\} = 0 \text{ at } y = 1 \text{ for } -1 \leq x \leq 1, \quad (42)$$

$$\{v_{1,1}, v_{2,1}\} = 0 \text{ at } y = k \text{ for } -1 \leq x \leq 1, \quad (43)$$

$$u_{1,1} = \mu_{12}u_{2,1} \text{ at } y = k \text{ for } -1 \leq x \leq 1, \quad (44)$$

$$\frac{\partial v_{1,1}}{\partial x} + \lambda \frac{\partial u_{1,1}}{\partial y} = \frac{\partial v_{2,1}}{\partial x} + \lambda \frac{\partial u_{2,1}}{\partial y} \text{ at } y = k \text{ for } -1 \leq x \leq 1. \quad (45)$$

The normal stress boundary condition yields

$$P_{1,1} - P_{2,1} + 2\lambda \left(\frac{\partial v_{2,1}}{\partial y} - \frac{\partial v_{1,1}}{\partial y} \right) = \frac{1}{Ca} \left(-\frac{\partial^2 f_1}{\partial x^2} \right) \text{ at } y = k \text{ for } -1 \leq x \leq 1. \quad (46)$$

Equations (35)–(37) describe a two dimensional, secondary flow. Hence, we adopt a stream function formulation and define ψ to satisfy (35),

$$u_{i,1} = \lambda \frac{\partial \psi_i}{\partial y}, \quad (47)$$

$$v_{i,1} = -\frac{\partial \psi_i}{\partial x}. \quad (48)$$

Substituting (47) and (48) in (36) and (37) and eliminating $P_{i,1}$, we obtain two biharmonic equations

$$\frac{\partial^4 \psi_i}{\partial x^4} + 2\lambda^2 \frac{\partial^4 \psi_i}{\partial x^2 \partial y^2} + \lambda^4 \frac{\partial^4 \psi_i}{\partial y^4} = -\lambda \text{Re}_i \frac{dw_{i,o}^2}{dy}. \quad (49)$$

Taking the reference of value for ψ_i as $\psi_i(-1, -1) = 0$, we recast the boundary conditions (39)–(45) in terms of ψ_i ,

$$\psi_1 = 0 \text{ at } x = \pm 1 \text{ for } -1 \leq y \leq k, \quad (50)$$

$$\psi_2 = 0 \text{ at } x = \pm 1 \text{ for } k \leq y \leq 1, \quad (51)$$

$$\psi_1 = 0 \text{ at } y = -1 \text{ for } -1 \leq x \leq 1, \quad (52)$$

$$\psi_2 = 0 \text{ at } y = 1 \text{ for } -1 \leq x \leq 1, \quad (53)$$

$$\frac{\partial \psi_1}{\partial x} = 0 \text{ at } x = \pm 1 \text{ for } -1 \leq y \leq k, \quad (54)$$

$$\frac{\partial \psi_2}{\partial x} = 0 \text{ at } x = \pm 1 \text{ for } k \leq y \leq 1, \quad (55)$$

$$\frac{\partial \psi_1}{\partial y} = 0 \text{ at } y = -1 \text{ for } -1 \leq x \leq 1, \quad (56)$$

$$\frac{\partial \psi_2}{\partial y} = 0 \text{ at } y = 1 \text{ for } -1 \leq x \leq 1, \quad (57)$$

$$\psi_1 = 0 \text{ at } y = k \text{ for } -1 \leq x \leq 1, \quad (58)$$

$$\psi_2 = 0 \text{ at } y = k \text{ for } -1 \leq x \leq 1, \quad (59)$$

$$\frac{\partial \psi_1}{\partial y} = \mu_{12} \frac{\partial \psi_2}{\partial y} \text{ at } y = k \text{ for } -1 \leq x \leq 1, \quad (60)$$

$$-\frac{\partial^2 \psi_1}{\partial x^2} + \lambda^2 \frac{\partial^2 \psi_1}{\partial y^2} = -\frac{\partial^2 \psi_2}{\partial x^2} + \lambda^2 \frac{\partial^2 \psi_2}{\partial y^2} \text{ at } y = k \text{ for } -1 \leq x \leq 1. \quad (61)$$

The system of Eqs. (49)–(61) form a coupled biharmonic equation system. The method of superposition, for solving a single biharmonic equation, has been discussed by Meleshko.²² In this paper, we extend the method to solve two simultaneous biharmonic equations, drawing on the theory of linear operators.²⁴ The detailed derivation is presented in the Appendix. The final expressions for the stream functions are given below

$$\begin{aligned} \psi_1 = & \sum_{m=1}^{\infty} \left(C_1 \cosh(\omega_{m,1}x) + C_2 x \sinh(\omega_{m,1}x) + S_1 \left(\frac{1}{\omega_{m,1}^4} + \frac{\cos(\pi x)}{(\pi^2 + \omega_{m,1}^2)^2} \right) \right) \phi_{y,1} \\ & + \sum_{n=1}^{\infty} \left(C_3 \cosh\left(\frac{\omega_n y}{\lambda}\right) + C_4 \sinh\left(\frac{\omega_n y}{\lambda}\right) + C_5 y \cosh\left(\frac{\omega_n y}{\lambda}\right) + C_6 y \sinh\left(\frac{\omega_n y}{\lambda}\right) \right) \phi_x, \end{aligned} \quad (62)$$

$$\begin{aligned} \psi_2 = & \sum_{m=1}^{\infty} \left(C_7 \cosh(\omega_{m,2}x) + C_8 x \sinh(\omega_{m,2}x) + S_2 \left(\frac{1}{\omega_{m,2}^4} + \frac{\cos(\pi x)}{(\pi^2 + \omega_{m,2}^2)^2} \right) \right) \phi_{y,2} \\ & + \sum_{n=1}^{\infty} \left(C_9 \cosh\left(\frac{\omega_n y}{\lambda}\right) + C_{10} \sinh\left(\frac{\omega_n y}{\lambda}\right) + C_{11} y \cosh\left(\frac{\omega_n y}{\lambda}\right) + C_{12} y \sinh\left(\frac{\omega_n y}{\lambda}\right) \right) \phi_x, \end{aligned} \quad (63)$$

$$\begin{aligned} S_1 = & \left(\frac{-64\text{Re}_1}{\pi^5} \right) \left(2A_{1,0}B_{1,0} \int_{-1}^k \cosh\left(\frac{\pi y}{\lambda}\right) \phi_{y,1} dy + 2A_{1,0} \int_{-1}^k \sinh\left(\frac{\pi y}{2\lambda}\right) \phi_{y,1} dy + \right. \\ & \left. 2B_{1,0} \int_{-1}^k \cosh\left(\frac{\pi y}{2\lambda}\right) \phi_{y,1} dy + (A_{1,0}^2 + B_{1,0}^2) \int_{-1}^k \sinh\left(\frac{\pi y}{\lambda}\right) \phi_{y,1} dy \right), \end{aligned} \quad (64)$$

$$\begin{aligned} S_2 = & \left(\frac{-64\text{Re}_2}{\pi^5} \right) \left(2A_{2,0}B_{2,0} \int_k^1 \cosh\left(\frac{\pi y}{\lambda}\right) \phi_{y,2} dy + 2A_{2,0} \int_k^1 \sinh\left(\frac{\pi y}{2\lambda}\right) \phi_{y,2} dy + \right. \\ & \left. 2B_{2,0} \int_k^1 \cosh\left(\frac{\pi y}{2\lambda}\right) \phi_{y,2} dy + (A_{2,0}^2 + B_{2,0}^2) \int_k^1 \sinh\left(\frac{\pi y}{\lambda}\right) \phi_{y,2} dy \right), \end{aligned} \quad (65)$$

$$\begin{aligned} \phi_x = & \cos\left(\frac{(2n-1)\pi x}{2}\right), \quad \phi_{y,1} = \left(\frac{2}{1+k}\right)^{1/2} \sin\left(\frac{m\pi(y-k)}{1+k}\right), \quad \phi_{y,2} = \left(\frac{2}{1-k}\right)^{1/2} \sin\left(\frac{m\pi(y-k)}{1-k}\right) \\ \omega_n = & \frac{(2n-1)\pi}{2} & \omega_{m,1} = \frac{m\pi\lambda}{1+k} & \omega_{m,2} = \frac{m\pi\lambda}{1-k} \\ \text{for } n = & 1, 2, 3\dots & \text{for } m = 1, 2, 3\dots & \text{for } m = 1, 2, 3\dots \end{aligned}$$

Here C_1 – C_{12} are arbitrary constants, which must be determined using the boundary conditions (50)–(61), as detailed in the Appendix.

The rate of convergence of (62) and (63) depends on both k and λ . We find that, to capture all the qualitative features of the solution, 2 terms of each series in (62) and (63) are sufficient at $k = 0$; whereas, 3 are required for $k = 0.2$ – 0.5 (or $k = -0.2$ to -0.5). Any further shift in the interface position at $O(\varepsilon^0)$ requires a larger number of terms.

2. Calculation of the interface shape

Calculation of the circulatory flow at first order did not require knowledge of the location of the interface, i.e., all the boundary conditions were applied at the zeroth order approximation to the interface position, $y = k$. Having determined the cross flow, we can calculate the normal stresses exerted by the fluids on the interface. Then the normal stress balance (14) can be used to determine the interface position at $O(\varepsilon^1)$. Thus the calculation of the flow field has been decoupled from the calculation of the interface position; this simplification is a result of the domain perturbation method.

The pressure distribution across the cross section, associated with the circulatory flow, may be determined by integrating either Eqs. (36) or (37). We choose to integrate (37) for its simplicity.

This results in

$$P_{1,1} = -\frac{1}{\lambda} \int \frac{\partial^3 \psi_{1,1}}{\partial x^3} dy - \lambda \frac{\partial^2 \psi_{1,1}}{\partial x \partial y} + D_1, \quad (66)$$

$$P_{2,1} = -\frac{1}{\lambda} \int \frac{\partial^3 \psi_{2,1}}{\partial x^3} dy - \lambda \frac{\partial^2 \psi_{2,1}}{\partial x \partial y} + D_2. \quad (67)$$

Here D_1 and D_2 are arbitrary constants. We choose $D_1 = 0$; thereby, setting a convenient reference value for the pressure field. The value of D_2 determines the pressure jump across the interface; this is related to the shape of the interface, via the normal stress balance, at $O(\varepsilon^1)$,

$$\frac{\partial^2 f_1}{\partial x^2} = Ca \left[\frac{1}{\lambda} \left(\int \frac{\partial^3 \psi_1}{\partial x^3} dy - \int \frac{\partial^3 \psi_2}{\partial x^3} dy \right) - \lambda \left(\frac{\partial^2 \psi_1}{\partial x \partial y} - \frac{\partial^2 \psi_2}{\partial x \partial y} \right) \right] + D_2 Ca. \quad (68)$$

Integrating (68), we obtain a solution with three arbitrary constants. The three boundary conditions necessary to obtain a unique solution are

$$\frac{df_1}{dx} = 0 \text{ at } x = \pm 1, \quad (69)$$

$$\frac{\int_{-1}^1 \int_{-1+k+\varepsilon f_1(x)}^1 (1 + \varepsilon x) dy dx}{\int_{-1}^1 \int_{-1}^1 (1 + \varepsilon x) dy dx} = \alpha. \quad (70)$$

Equation (69) specifies the contact angle at both walls as 90° . Equation (70) ensures that the interface shape satisfies the input specification of the holdup (volume fraction) of fluid 2. Further simplification of (70) results in the following:

$$\frac{2(1-k) + \varepsilon \int_{-1}^1 f_1 dx + \varepsilon^2 \int_{-1}^1 f_1 x dx}{4} = \alpha. \quad (71)$$

The third term in the numerator of (71) represents the increase in volume of a differential element, as we move from the inner to the outer wall of a curved channel. This is a second order effect, however, and is neglected at $O(\varepsilon^1)$. Using (33a), we obtain

$$\frac{2(1-k) + \varepsilon \int_{-1}^1 f_1 dx}{4} = \frac{2(1-k)}{4}, \quad (72)$$

which results in the following condition on the interface deflection function $f_1(x)$:

$$\int_{-1}^1 f_1 dx = 0. \quad (73)$$

Solving (68), subject to the boundary conditions (69) and (73), determines simultaneously the shape of the interface and the pressure distribution. The corresponding analytical expressions are lengthy and not reproduced here.

The inhomogeneous term in (68) and the boundary conditions (69) and (73) imply that $f_1(x)$ is an odd function of x . Thus, the deformation of the interface is anti-symmetric (equal and opposite) about the y -axis.

We conclude this subsection by considering the limiting case of strong capillary forces, i.e., $Ca \rightarrow 0$. In this limit, Eq. (68) simplifies to

$$\frac{\partial^2 f_1}{\partial x^2} = 0, \quad (74)$$

which along with the homogeneous boundary conditions (69) and (73) yields the trivial solution

$$f_1 = 0. \quad (75)$$

Hence in the limit of low capillary numbers (high surface tension and small channel dimensions), capillary forces overcome the normal stresses and keep the interface flat. For small but finite values of Ca , the interface deformation will be small and can be accurately described by the perturbation solution presented here. This situation is common in microchannel flows.

3. Calculation of the flow rates at the first order

The flow rates of the fluids in a curved channel are expected to differ from those in a straight channel. The factors which may affect the flow rate are: (i) the change in the flow area due to the deformation of the interface and (ii) the axial velocity correction ($w_{i,1}$). In this section, we show that the change to the flow rates is relatively small, of $O(\varepsilon^2)$; i.e., the change is zero at $O(\varepsilon^1)$. This calculation is of practical significance, as the flow rates are more easily controlled in an experiment than the pressure drop and holdup.

As a precursor to the flow rate calculation, we determine the axial velocity correction at $O(\varepsilon^1)$. This requires solving (38) for $w_{i,1}$, subject to the following boundary conditions:

$$w_{1,1} = 0 \text{ at } x = \pm 1 \text{ for } -1 \leq y \leq k, \quad (76)$$

$$w_{2,1} = 0 \text{ at } x = \pm 1 \text{ for } k \leq y \leq 1, \quad (77)$$

$$w_{1,1} = 0 \text{ at } y = -1 \text{ for } -1 \leq x \leq 1, \quad (78)$$

$$w_{2,1} = 0 \text{ at } y = 1 \text{ for } -1 \leq x \leq 1, \quad (79)$$

$$w_{1,1} + f_1 \frac{\partial w_{1,0}}{\partial y} = \mu_{12} \left(w_{2,1} + f_1 \frac{\partial w_{2,0}}{\partial y} \right) \text{ at } y = k \text{ for } -1 \leq x \leq 1, \quad (80)$$

$$\frac{\partial w_{1,1}}{\partial y} + f_1 \frac{\partial^2 w_{1,0}}{\partial y^2} = \frac{\partial w_{2,1}}{\partial y} + f_1 \frac{\partial^2 w_{2,0}}{\partial y^2} \text{ at } y = k \text{ for } -1 \leq x \leq 1. \quad (81)$$

The solution procedure is similar to that used for obtaining $w_{i,0}$, except that the inhomogeneous terms are functions of x and y . We seek a solution of the following form, which is an odd function of x :

$$w_{i,1} = \sum_{n=1}^{\infty} g_{i,n}(y) \sin(n\pi x). \quad (82)$$

The coefficients $g_{i,n}(y)$ are obtained by solving the following ordinary differential equations:

$$\begin{aligned} \text{Re}_i \left(\int_{-1}^1 u_{i,1} \frac{\partial w_{i,0}}{\partial x} \sin(n\pi x) dx + \int_{-1}^1 \lambda v_{i,1} \frac{\partial w_{i,0}}{\partial y} \sin(n\pi x) dx \right) \\ - \int_{-1}^1 \frac{\partial w_{i,0}}{\partial x} \sin(n\pi x) dx = -(n\pi)^2 g_{i,n} + \lambda^2 \frac{d^2 g_{i,n}}{dy^2}. \end{aligned} \quad (83)$$

The analytical expressions for $g_{i,n}(y)$ are obtained using Mathematica and are not reproduced here, owing to their length.

The flow rates are obtained by integrating w_i over the domain of each fluid

$$Q_1 = \int_{-1}^1 \int_{-1}^{k+\varepsilon f_1} w_{1,0}(1 + \varepsilon x) dy dx + \int_{-1}^1 \int_{-1}^{k+\varepsilon f_1} \varepsilon w_{1,1}(1 + \varepsilon x) dy dx, \quad (84)$$

$$Q_2 = \int_{-1}^1 \int_{k+\varepsilon f_1}^1 w_{2,0}(1 + \varepsilon x) dy dx + \int_{-1}^1 \int_{k+\varepsilon f_1}^1 \varepsilon w_{2,1}(1 + \varepsilon x) dy dx. \quad (85)$$

Expanding (84) yields

$$Q_1 = \int_{-1}^1 \int_{-1}^{k+\varepsilon f_1} (w_{1,0} + \varepsilon w_{1,1}) dy dx + \varepsilon \int_{-1}^1 \int_{-1}^{k+\varepsilon f_1} x w_{1,0} dy dx + \varepsilon^2 \int_{-1}^1 \int_{-1}^{k+\varepsilon f_1} x w_{1,1} dy dx. \quad (86)$$

The third term in (86) accounts for the increasing volume of a differential element, as one moves from the inner to the outer wall, in a curved channel. However, this is a second order effect and is neglected at $O(\varepsilon^1)$. The integrand in the second term is an odd function of x ; it reduces to zero on integrating over the channel's width. This leaves the first term, which after expansion as a Taylor series about $\varepsilon = 0$, yields

$$Q_1 = \int_{-1}^1 \int_{-1}^k w_{1,0} dy dx + \varepsilon \frac{\partial}{\partial \varepsilon} \int_{-1}^1 \int_{-1}^{k+\varepsilon f_1} (w_{1,0} + \varepsilon w_{1,1}) dy dx. \quad (87)$$

The first term in (87) is the flow rate at $O(\varepsilon^0)$ – the case of a straight channel; the second term is the change that occurs in a curved channel (ΔQ_1),

$$\Delta Q_1 = \varepsilon \frac{\partial}{\partial \varepsilon} \int_{-1}^1 \int_{-1}^{k+\varepsilon f_1} (w_{1,0} + \varepsilon w_{1,1}) dy dx \Big|_{\varepsilon=0}, \quad (88)$$

$$\Delta Q_1 = \varepsilon \frac{\partial}{\partial \varepsilon} \int_{-1}^1 \int_{-1}^{k+\varepsilon f_1} w_{1,0} dy dx \Big|_{\varepsilon=0} + \varepsilon \int_{-1}^1 \int_{-1}^k w_{1,1} dy dx + \varepsilon^2 \frac{\partial}{\partial \varepsilon} \int_{-1}^1 \int_{-1}^{k+\varepsilon f_1} w_{1,1} dy dx \Big|_{\varepsilon=0}. \quad (89)$$

Neglecting the second order term and applying Leibnitz rule on the first term yields

$$\Delta Q_1 = \varepsilon \int_{-1}^1 w_{1,0}(x, k) f_1(x) dx + \varepsilon \int_{-1}^1 \int_{-1}^k w_{1,1}(x, y) dy dx. \quad (90)$$

Both these integrands are odd functions of x which reduce to zero on integrating over $[-1, +1]$. Physically, the first term represents the change in flow rate due to interface deformation; whereas, the second term represents the change due to the first order axial velocity correction. Since both these features are anti-symmetric about $x = 0$, an increase in the flow rate, through one lateral half of the channel, is compensated by an equivalent decrease, in the other half. Similar calculations show that the flow rate change for phase 2 at $O(\varepsilon^1)$ is also zero. Thus we have

$$Q_1 = \int_{-1}^1 \int_{-1}^k w_{1,0} dy dx + O(\varepsilon^2), \quad (91)$$

$$Q_2 = \int_{-1}^1 \int_{-k}^1 w_{2,0} dy dx + O(\varepsilon^2). \quad (92)$$

Dean²⁵ and Cuming² also found no change in the flow rate at $O(\varepsilon^1)$, for single-phase flow through curved, circular, and rectangular channels, respectively. However, they report a decrease in the flow rate at $O(\varepsilon^2)$. This decrease occurs due to the extra energy expended in driving the circulatory flow. We expect to find a similar effect in the two phase problem, at $O(\varepsilon^2)$, as well.

Equations (91) and (92) are explicit formulae for the flow rates, in terms of the holdup and pressure drop (G in the definition of the Reynolds numbers). If the flow rates are specified, then the

flow field can be calculated iteratively, starting from guess values of the pressure drop and holdup, using (91) and (92).

IV. FLOW PATTERNS

In this section, we present different circulatory flow patterns, obtained as the parameters are varied. We also identify the two key factors which are responsible for generating these patterns.

Before examining the two-phase flow field, it is instructive to review the circulatory flow in the single-phase case.^{1,2} The circulatory flow, for a single fluid flowing through a gently curved channel, consists of two counter rotating helical vortices, as shown in Fig. 2. For ease of visualization, we project the streamlines of the flow onto the x - y plane (cross-section of the channel). The helical flow then appears as two-dimensional vortices. These counter rotating vortices form because the centrifugal forces are much stronger along the central horizontal plane, $y = 0$, where the axial velocity is maximum- the magnitude of the centrifugal force is proportional to the square of the axial velocity. On the other hand, the centrifugal forces are much lower near the top and bottom walls, where the axial velocity approaches zero. Thus, fluid is thrown out strongly along the center of the channel and recirculates along the walls. This leads to the formation of a pair of counter-rotating vortices on either side of $y = 0$.

Generalizing the relationship between the maximum of the base axial velocity and the vortex location, we deduce the following: the separatrix (line of separation) between the pair of counter rotating vortices corresponds closely to the location of the maximum base axial velocity. In the single-phase case, this maximum always lies at the center of the channel (i.e., $y = 0$). However in two-phase flow, the base, axial velocity profile is generally asymmetric; it depends on the viscosities and holdup (volume fraction) of the fluids, and the maximum may lie in either fluid. This leads to the generation of new circulation patterns. Further, if the two fluids happen to flow in opposite directions near the interface, then inter-fluid shear interaction comes into play. These two mechanisms lead to a variety of flow patterns, which are discussed subsequently. Each pattern is denoted by a unique two-tuple label (#-#); the two entries represent the number of vortices in the first and second fluid, respectively.

A. Identification of flow patterns

1. 1-1 Configuration

Consider the situation when the maxima of the base axial velocity lies near the interface (Fig. 3(a)); then the centrifugal force has the strongest impact near the interface. Therefore, both fluids flow outward along the interface, in the direction of the centrifugal force, and recirculate along the top and bottom walls. Thus two vortices are formed, one in each fluid, which have an opposite

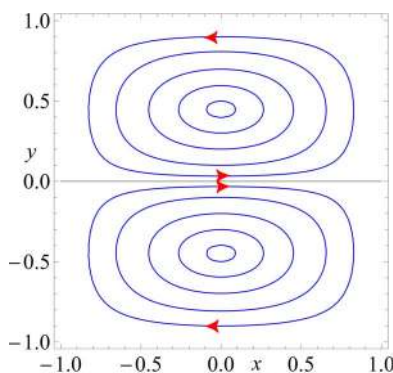


FIG. 2. The secondary circulations in single-phase flow through a gently curved channel. These are called Dean vortices. Here the streamlines of the flow are projected onto the x - y plane; the helical Dean flow appears as two-dimensional vortices.

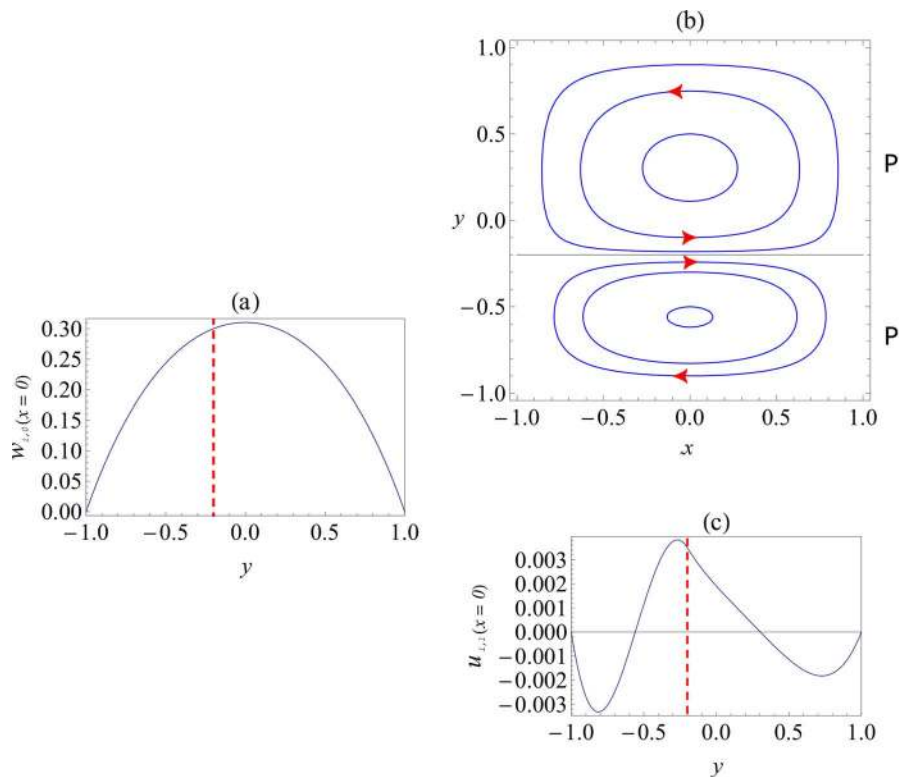


FIG. 3. (a) Variation of the axial velocity at zeroth order ($w_{i,0}$) across the height of the channel (y). The maxima of the axial velocity lies near the interface, in phase 2. (b) 1–1 Configuration: One principal vortex (P) is present in each phase. (c) Variation of the x -component of velocity at first order ($u_{i,1}$), at $x = 0$, across the height of the channel (y). The system parameters are $\mu_{12} = 1$, $Re_1 = 5$, $Re_2 = 1$, $k = -0.2$, $\lambda = 1$. The location of streamlines in (b) have been chosen to best illustrate the circulation pattern. The magnitude of the cross flow may be gauged from the plot of $u_{i,1}$ in (c).

sense of rotation (Fig. 3(b)). These vortices resemble those in the single phase case (cf. Fig. 2); they are called *principal vortices*, and labeled “P.” The magnitude of the cross flow, in each fluid, may be gauged from the plot of $u_{i,1}$ at $x = 0$ along y (Fig. 3(c)). The zeros of $u_{i,1}$ ($x = 0$) within each fluid domain correspond to the two vortex centers. In this case the fluids flow in the same direction at the interface, and inter-fluid interaction is irrelevant. This 1–1 configuration is the only flow pattern which has been reported previously (by Gelfgat *et al.*⁹).

2. 1–3 Configuration

Next, we examine a case wherein the maximum of the base axial velocity lies away from the interface, within fluid 2 (Fig. 4(a)). The centrifugal force is now strongest within the bulk of fluid 2; this creates a pair of counter rotating vortices in fluid 2 itself. This pair of vortices are named *split vortices* – labelled “SP” (Fig. 4(b)). In fluid 1, the situation remains the same as in the 1–1 configuration – a single principle vortex is present. However, the principle vortex in fluid 1 has the same sense of rotation as the lower split vortex in fluid 2. This would result in opposing directions of flow at the interface – violating continuity of the velocity field. The situation is resolved by the presence of an intermediate vortex which preserves the continuity of the velocity field at the interface. This vortex is called a sandwich vortex – labelled “SW.” In this case it is located in fluid 2 (Fig. 4(b)). Thus, we have a total of four vortices: one in phase 1 and three in phase 2 (Fig. 4(b)). Corresponding to these vortex centers, $u_{i,1}(x = 0)$ has four zeros within the fluid domains (cf. Fig. 4(c)).

Sandwich vortices arise whenever there is a tendency for fluid to flow in opposite directions, at an interface. These were studied by Picardo and Pushpavanam¹⁰ in the context of core-annular flow

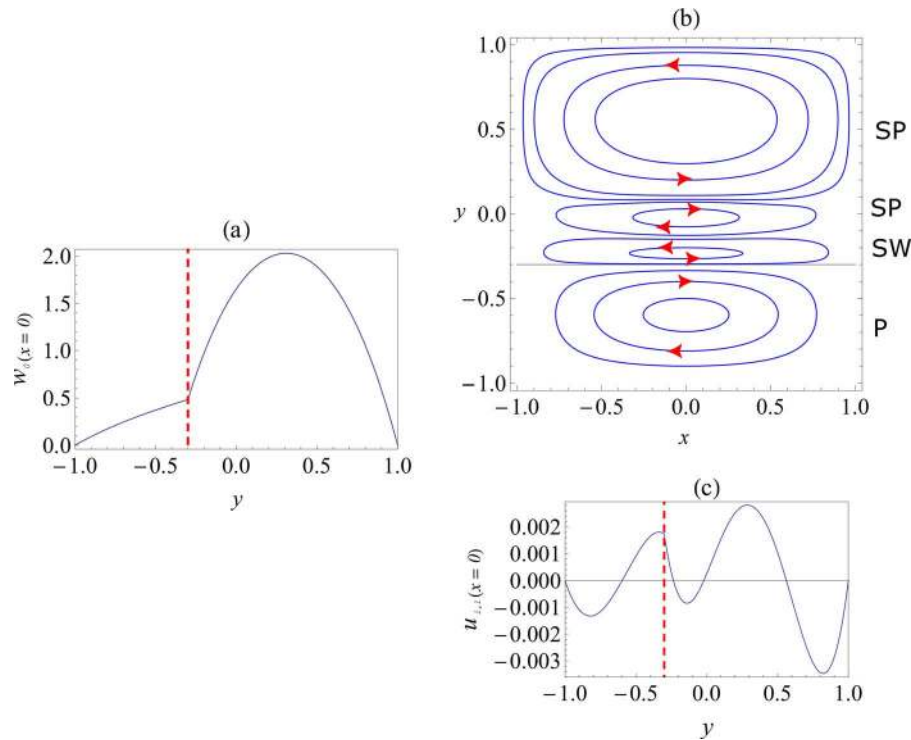


FIG. 4. (a) Variation of the axial velocity at zeroth order ($w_{i,0}$) across the height of the channel (y). The maxima of the axial velocity is in phase 2, away from the interface. (b) 1–3 Configuration: The principal vortex (P) is present in phase 1. A pair of split vortices (SP) and a sandwich vortex (SW) is present in phase 2. (c) Variation of the x -component of velocity at first order ($u_{i,1}$), at $x = 0$, across the height of the channel (y). The system parameters are $\mu_{12} = 10$, $Re_1 = 1$, $Re_2 = 1$, $k = -0.3$, $\lambda = 1$.

in curved channels. The sandwich vortex may be present in either fluid, depending on the parameter values. In fact, their location is related to a competition between the two fluids. The sandwich vortex corresponds to a local reversal of flow; the fluid within the sandwich vortex is forced to circulate against its natural tendency. Thus in the case of the 1–3 pattern, fluid 1 controls the flow locally near the interface, forcing fluid 2 to form a sandwich vortex. This is in spite of fluid 2 having a stronger average circulatory flow.

Two key ideas have been introduced here, to explain the 1–3 configuration: (i) the creation of counter-rotating split vortices within one of the fluids, when the maximum of $w_{i,0}$ is located away from the interface (ii) the creation of sandwich vortices, due to inter-fluid stress interaction, when the fluids have a tendency to flow in opposite directions at the interface. These two mechanisms are sufficient to explain, and anticipate, all the other flow configurations observed in this system.

3. 1–2 Configuration

In the previous, 1–3 pattern, fluid 1 controls the flow at the interface, causing a sandwich vortex to form in fluid 2. As parameters are varied, the influence of fluid 1 on fluid 2 can decrease; this will cause the size of the sandwich vortex to reduce. Ultimately, the sandwich vortex will disappear, resulting in a 1–2 configuration as depicted in Fig. 5. Here fluid 2 has a pair of split vortices (Figs. 5(b) and 5(c)), since the maximum of $w_{i,0}$ is still located within fluid 2 (Fig. 5(a)). Fluid 1 contains only a principle vortex (Figs. 5(b) and 5(c)). In this case, the x component of velocity ($u_{i,1}$) is identically zero at the interface, to maintain continuity of velocity, while fluid flows in opposite directions on either side of the interface (Fig. 5(c)). This situation represents a perfect balance between the two fluids at the interface, with neither fluid controlling the flow.

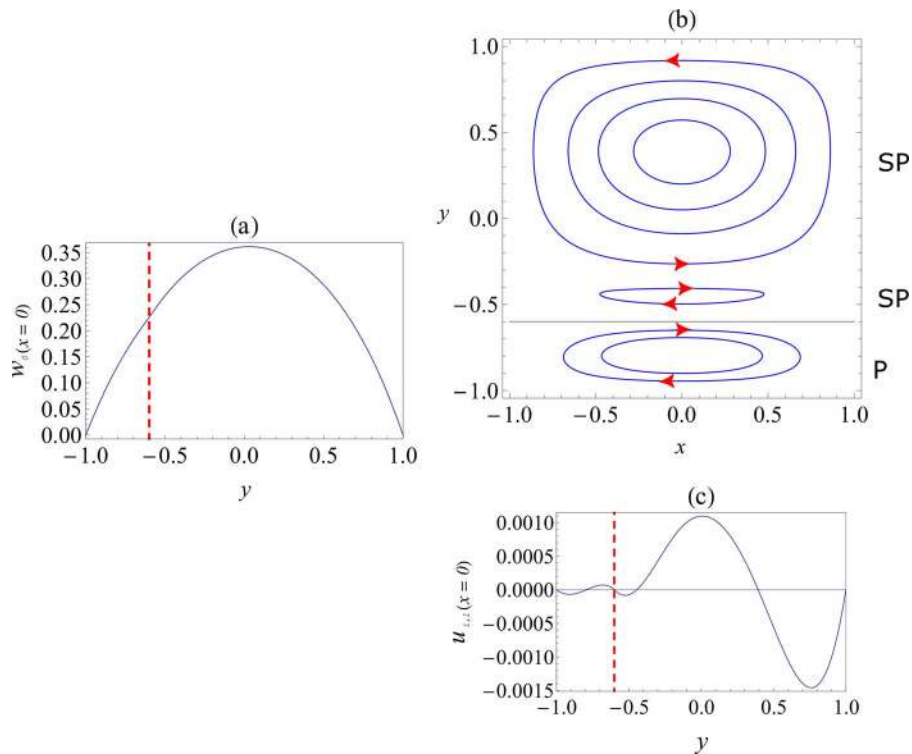


FIG. 5. (a) Variation of the axial velocity at zeroth order ($w_{i,0}$) across the height of the channel (y). The maximum of the base axial velocity is in phase 2. (b) 1–2 Configuration: The principal vortex (P) is present in phase 1, and a pair of split vortices (SP) is present in phase 2. (c) Variation of the x -component of velocity at first order ($u_{i,1}$), at $x = 0$, across the height of the channel (y). The system parameters are $\mu_{12} = 1.2$, $Re_1 = 1$, $Re_2 = 1$, $k = -0.6$, $\lambda = 1$.

4. 2–2 Configuration

In this configuration, fluid 2 controls the flow near the interface, while containing the maximum $w_{i,0}$ (Fig. 6(a)). Thus we have a 2–2 configuration: fluid 2 has a pair of split vortices, while fluid 1 contains a principle vortex along with a sandwich vortex near the interface (Figs. 6(b) and 6(c)). On comparing this configuration with the previous two – 1–3, 1–2, and 2–2 configurations – we observe that the sandwich vortex shifts from fluid 2 into fluid 1. Thus, the 1–2 pattern represents a transition between the 1–3 pattern and the 2–2 configuration, i.e., a transition between a regime where fluid 1 controls the flow at the interface to a regime in which fluid 2 is dominant.

5. 1(R)-2 Configuration

In this configuration, fluid 2 completely dominates the flow within fluid 1; the sandwich vortex, which was localized near the interface in the 2–2 configuration, now occupies the entire region of fluid 1 (compare the vortices in Figs. 6(b) and 7(b)). All the fluid in phase 1 is now forced to circulate against its natural tendency, as is evident from a comparison of the flow in the present case (Fig. 7) with the 1–2 configuration (Fig. 5) – the single vortex (in phase 1) in Fig. 7(b) circulates in an opposite direction to the principle vortex in Fig. 5(b). (This change of direction is confirmed by the derivative of $u_{i,1}(x=0)$ at its zero within phase 1 – it has a different sign in Figs. 5(c) and 7(c).) This reversal of the flow in fluid 1 is caused by the dominating influence of fluid 2, via stress interaction at the interface. The resultant vortex in fluid 1 is called a reversed vortex – labeled “R,” and the flow pattern is called the 1(R)-2 configuration. It contains a reversed vortex in fluid 1 and a pair of split vortices in fluid 2 (Fig. 7(b)).

Thus far, we have described one pattern in which the maximum of the base axial velocity was near the interface and four patterns where the maximum was in the bulk of fluid 2. Apart from these,

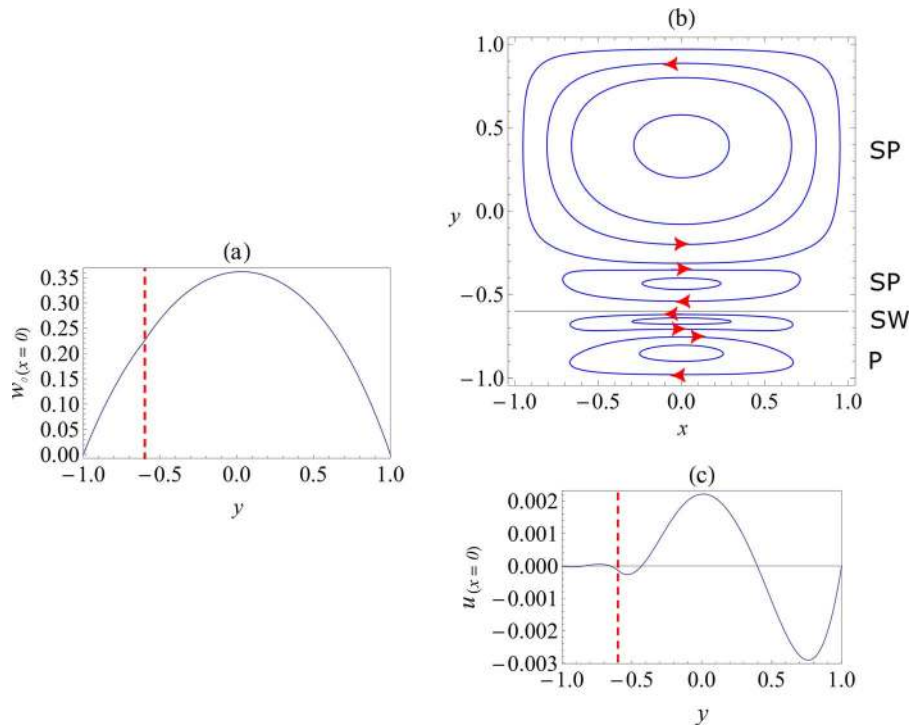


FIG. 6. (a) Variation of the axial velocity at zeroth order ($w_{i,0}$) across the height of the channel (y): The maximum of the base axial is in phase 2. (b) 2–2 Configuration: The sandwich (SW) and the principal vortex (P) is in phase 1; the pair of split vortices (SP) is in phase 2. (c) Variation of the x -component of velocity at first order ($u_{i,1}$), at $x = 0$, across the height of the channel (y). The system parameters are $\mu_{12} = 1.2$, $Re_1 = 1$, $Re_2 = 2$, $k = -0.6$, $\lambda = 1$.

four more patterns occur when the maximum is located in the bulk of fluid 1. These four are similar to those described above, and are related by an inversion of phases. They are listed below, with a brief description relating them to their inverse counterparts.

6. 3–1 Configuration

This is the inverse of the 1–3 configuration (cf. Fig. 4(b)). Split vortices are created within fluid 1 (Fig. 8(a)). Fluid 2 has a single principle vortex. The flow at the interface is controlled by fluid 2; hence a sandwich vortex is present in fluid 1 (Fig. 8(a)).

7. 2–1 Configuration

Here the size of the sandwich vortex of the 3–1 pattern has shrunk to zero; the velocity is identically zero at the interface, while the fluids flow in opposite directions on either side. Thus, a pair of split vortices are present in fluid 1, while fluid 2 has a single principle vortex (Fig. 8(b)). This is the inverse of the 1–2 configuration (cf. Fig. 5(b)).

8. 2–2(s) Configuration

In this pattern, the sandwich vortex is located in fluid 2, while the split vortices are present in fluid 1 (Fig. 8(c)). Fluid 1, therefore, controls the flow at the interface. This pattern has been called 2–2(s)- the (s) is added to distinguish it from its inverse 2–2 pattern (cf. Fig. 6(b)).

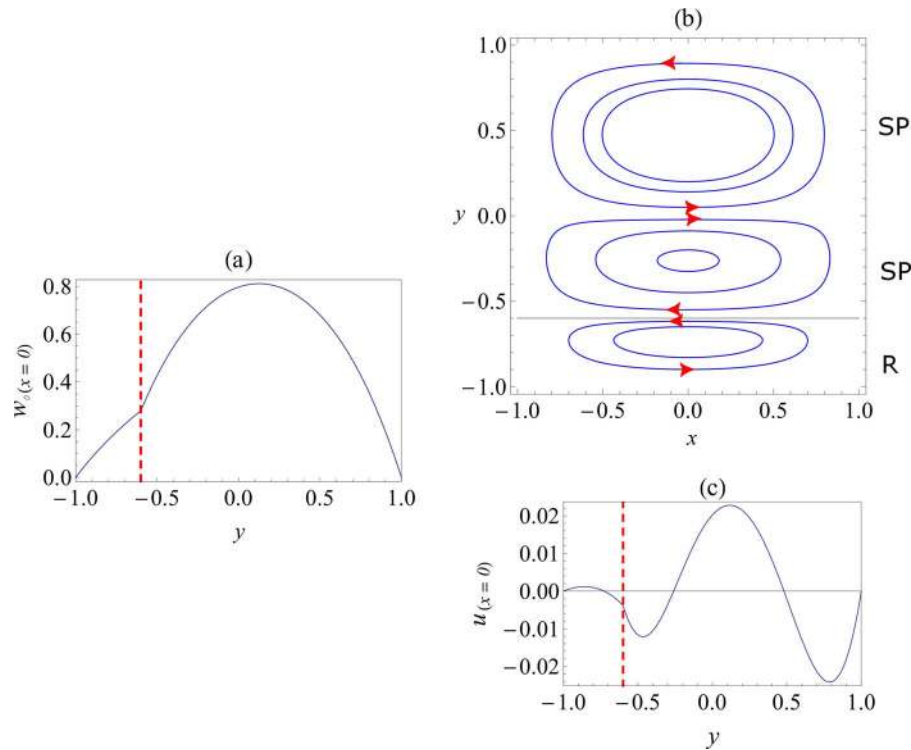


FIG. 7. (a) Variation of the axial velocity, at zeroth order ($w_{i,0}$), across the height of the channel (y). The maximum of centrifugal force is in phase 2. (b) 1(R)-2 Configuration: Fluid 1 contains a reversed vortex (R) (a sandwich vortex occupying the entire phase); fluid 2 contains a pair of split vortices (SP). (c) Variation of the x -component of velocity at first order ($u_{i,1}$), at $x = 0$, across the height of the channel (y). The system parameters are $\mu_{12} = 3$, $Re_1 = 1$, $Re_2 = 10$, $k = -0.6$, $\lambda = 1$.

9. 2-1(R) Configuration

In this case, fluid 2 contains a reversed vortex; it is forced to circulate against its natural tendency, under the influence of fluid 1. Fluid 1 itself contains a pair of split vortices (Fig. 8(d)). This pattern is the inverse of the 1(R)-2 configuration (cf. Fig. 7(b)).

10. Classification of the flow patterns

The nine different flow patterns just described can be classified into three groups, based on the location of the maximum of the base axial velocity ($w_{i,0}$):

- *Type 1*: The maximum of the base axial velocity ($w_{i,0}$) is near the interface, in either of the fluids. Only the 1-1 configuration, with two principle vortices, belongs to this category.
- *Type 2*: The maximum of $w_{i,0}$ is in the bulk of phase 2, far from the interface. 1-3, 1-2, 2-2, and 1(R)-2 flow configurations belong to this category. Apart from generating split vortices, the presence of the maximum in fluid 2 results in stronger centrifugal forces; thus the average circulatory flow is stronger in fluid 2. However, near the interface, the flow can be controlled by either fluid 1 or 2. This inter-fluid competition is evident in the location of the sandwich/reversed vortex. Fluid 1 controls the flow along the interface in the 1-3 pattern, while fluid 2 plays a dominating role in the other three flow configurations.
- *Type 3*: The maximum of $w_{i,0}$ is in the bulk of phase 1, far from the interface. The 3-1, 2-1, 2-2(s), and 2-1(R) flow configurations belong to this category. The average circulatory flow is stronger in fluid 1, in all cases. The flow, in the vicinity of the interface, is controlled by fluid 2 in the 3-1 pattern; whereas, fluid 1 is dominant in the other three cases.

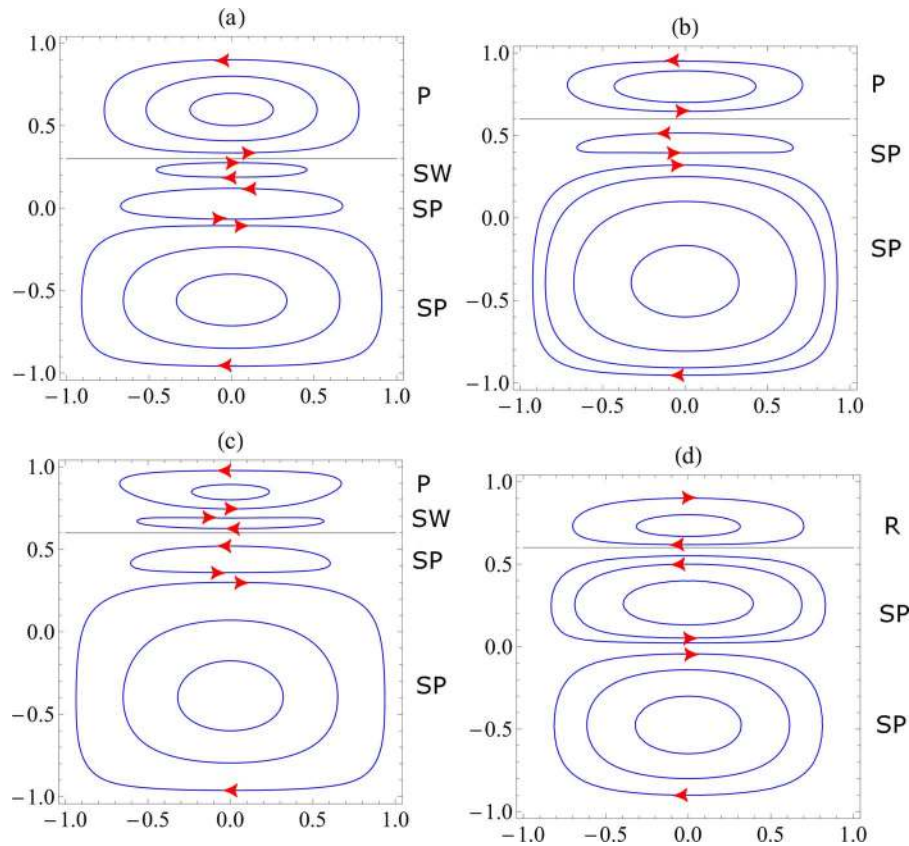


FIG. 8. (a) 3–1 Configuration: $\mu_{12} = 1/10$, $Re_1 = 1$, $Re_2 = 1$, $k = 0.3$, $\lambda = 1$; (b) 2–1 Configuration: $\mu_{12} = 1/1.2$, $Re_1 = 1$, $Re_2 = 1$, $k = 0.6$, $\lambda = 1$; (c) 2–2(s) Configuration: $\mu_{12} = 1/1.2$, $Re_1 = 2$, $Re_2 = 1$, $k = 0.6$, $\lambda = 1$; (d) 2–1(R) Configuration: $\mu_{12} = 1/3$, $Re_1 = 10$, $Re_2 = 1$, $k = 0.6$, $\lambda = 1$.

In this section, we have identified and classified different types of circulatory patterns which can occur in vertically stratified curved channel flow at low Reynolds numbers. This diversity of flow patterns has been explained in terms of inter-fluid competition and the location of the maximum base axial velocity ($w_{i,0}$). In Sec. V, we discuss how these two factors can be manipulated by varying the parameters of the system. Thus, the parameter values which correspond to different flow patterns may be identified – the parameters for the examples depicted in Figs. 3–8 were chosen on this basis.

The circulatory flow field studied in this section does not include any effects of the deformed interface. This effect occurs at the higher order of ε^2 ; thus the flow at $O(\varepsilon)$ is plotted on the base domain with an undeformed interface. The effect of interface deformation will be relatively small and localized near the interface, when ε is small. It can be ignored to a good approximation at low capillary numbers, when the interface deformation itself is very small (cf. Sec. VII).

V. ORGANIZATION OF THE PARAMETER SPACE (μ_{12} , Re_1 , Re_2 , and k)

In this subsection, we focus on identifying regions of the parameter space in which different flow patterns occur. First, we demonstrate an efficient method for constructing flow regime maps, using our analytical asymptotic solution. Then, these maps are used to understand the effect of the parameters on the flow field. This requires an understanding of the effect of parameter variations on the two mechanisms governing the flow patterns: the location of the maximum base axial velocity ($w_{i,0}$) and the inter-fluid competition.

A. Flow regime maps

The flow regime maps are constructed by locating the boundaries, in parameter space, between different flow patterns. These boundaries can be determined precisely by identifying special characteristic features of the plot of $u_{i,1}$ at $x = 0$, at the transition between flow patterns. These line plots (cf. Figs. 3(c) and 4(c)–7(c)) contain key information about the flow field. The zeros of the plot, within the domain of the fluids, correspond to vortex centers; the derivative at these zeros indicate the sense of rotation of the vortex – a negative derivative corresponds to counter-clockwise rotation, while a positive derivative represents a clockwise vortex. We now present conditions on the profile of $u_{i,1}(x = 0)$ which must be satisfied at the transition between various flow patterns. These conditions, in conjunction with our analytical result for $u_{i,1}$, can be used to efficiently map out the parameter space.

Since the Type-2 (maximum of $w_{i,0}$ in phase 2) and Type-3 (maximum of $w_{i,0}$ in phase 1) configurations are in a one-to-one correspondence – related by swapping the two fluids – we discuss only the transitions between Type 1 and Type 2 patterns in detail. The boundaries between different Type 3 flow patterns are then obtained analogously.

1. Boundary between 1–1 and 1–3 configurations

Observing Fig. 4(c) – the plot of $u_{i,1}(x = 0)$ for the 1–3 configuration – we find a local minimum near the interface in fluid 2, which has a negative value. There are two zeros on either side of this local minimum, which correspond to vortex centers: the one near the interface is the sandwich vortex, and the one away from the interface is the lower split vortex. Now, as the value of $u_{2,1}(x = 0)$ at this minimum increases, the two zeros approach each other; they eventually merge into a double root, when the local minimum has a value of zero. Any further increase in the local minimum leads to the disappearance of the two vortices, and we have the 1–1 configuration (e.g., Fig. 3(c)). Thus, the boundary between the 1–1 and 1–3 patterns is characterized by the following double zero condition within fluid 2:

$$\frac{\partial u_{2,1}}{\partial y} = 0 \text{ and } u_{2,1} = 0 \text{ at } x = 0. \quad (93)$$

These two equations can be solved simultaneously to determine the location of the double root and the value of any one parameter at the transition, for specified values of the other parameters. Since we have four physical parameters (apart from the geometric parameters) – μ_{12} , Re_1 , Re_2 , and k – the transition boundary determined by (93) is a three dimensional manifold in a four dimensional parameter space.

2. Boundary between 1–3 and 2–2 configurations

In the 1–3 pattern the sandwich vortex is present in fluid 2 (Fig. 4); whereas, in the 2–2 configuration the sandwich vortex is in fluid 1 (Fig. 6). At the critical boundary between these two cases, the sandwich vortex disappears; it is in neither fluid. This is precisely the situation in the 1–2 configuration (Fig. 5). At this transition pattern, the velocity at the interface must be identically zero, to maintain continuity of the velocity field (Fig. 5(c)). In terms of $u_{i,1}(x = 0)$, the 1–3 configuration has a sandwich vortex zero near the interface, in fluid 2 (Fig. 4(c)); whereas, the 2–2 pattern has a sandwich vortex zero in fluid 1 (Fig. 6(c)). In the 1–2 transition pattern, the corresponding zero is located exactly at $y = k$ (Fig. 5(c)). Thus we have the following condition for the boundary between 1–3 and 2–2:

$$u_{1,1} = u_{2,1} = 0 \text{ at } y = k \text{ at } x = 0. \quad (94)$$

This equation can be solved to determine any one parameter, when the values of all others are fixed. Thus (94) represents a three dimensional manifold in the four dimensional parameter space.

3. Boundary between 2–2 and 1(R)-2 configurations

At the transition from the 2–2 pattern (Fig. 6) to the 1(R)-2 pattern (Fig. 7), the principle vortex near the lower wall in fluid 1 shrinks and disappears (Fig. 6(b)). The corresponding zero of $u_{1,1}(x=0)$ moves closer to the lower wall ($y=-1$) and ultimately coincides with the wall at the transition. However, $u_{1,1}$ is always zero at the wall due to the no-slip condition. Hence, at the transition, we have a double root at the lower wall

$$\frac{\partial u_{1,1}}{\partial y} = 0 \text{ at } y = -1 \text{ at } x = 0. \quad (95)$$

Like (94), this equation can be solved to determine any one parameter, when the values of all others are fixed. Thus (95) also represents a three dimensional manifold in the four dimensional parameter space.

4. Boundaries between Type 3 patterns

The boundaries between different Type 3 flow patterns are characterized by conditions, entirely analogous to those for the Type 2 patterns. The same arguments apply, but with an interchange of the two fluids. These conditions are listed below.

Boundary between the 1–1 configuration and the 3–1 configuration:

$$\frac{\partial u_{1,1}}{\partial y} = 0 \text{ and } u_{1,1} = 0 \text{ at } x = 0. \quad (96)$$

Boundary between the 3–1 configuration and the 2–2(s) configuration, which corresponds to the 2–1 pattern

$$u_{1,1} = u_{2,1} = 0 \text{ at } y = k \text{ at } x = 0. \quad (97)$$

Boundary between the 2–2(s) configuration and the 2–1(R) configuration

$$\frac{\partial u_{2,1}}{\partial y} = 0 \text{ at } y = +1 \text{ at } x = 0. \quad (98)$$

5. Flow regime maps in the $Re_1 - \mu_{12}$ parameter plane

We now fix the values of two parameters – the volume fraction (k) and one of the Reynolds numbers – and construct flow regime maps in the parameter plane of the remaining two parameters, using conditions (93)–(98).

In Fig. 9(a), the parameter regions for Type 1 and Type 2 patterns are identified in the $Re_2 - \mu_{12}$ plane, for the case of $k = -0.2$, $Re_1 = 1$. The three conditions, (93)–(95), define three curves in the $Re_2 - \mu_{12}$ plane, that divide it into four regions. These regions correspond to different circulation patterns (Type 1 and Type 2), as indicated in Fig. 9(a). The boundaries between Type 3 patterns can also be plotted in this figure; however, they occur at physically unrealistic value of Re_2 and μ_{12} . Instead, we plot another flow regime map (Fig. 9(b)) for the opposite case of $k = +0.2$, $Re_2 = 1$. This map in the $Re_1 - \mu_{12}$ plane reveals the boundaries between Type 1 and Type 3 flow configurations, as obtained from conditions (96)–(98).

Flow regime maps, similar to those in Fig. 9, can be easily constructed for any parameter range of interest. Once two parameter values are fixed, Eqs. (93)–(98) must be solved to yield relationships between the remaining two parameters. To generate Fig. 9, Eqs. (93) and (96) were solved numerically, while the other conditions were solved analytically.

B. Influence of parameter variations

On the basis of the flow regime maps in Fig. 9 and the results presented in Sec. IV, we proceed to discuss the influence of each parameter on the flow pattern. Transitions between flow patterns are

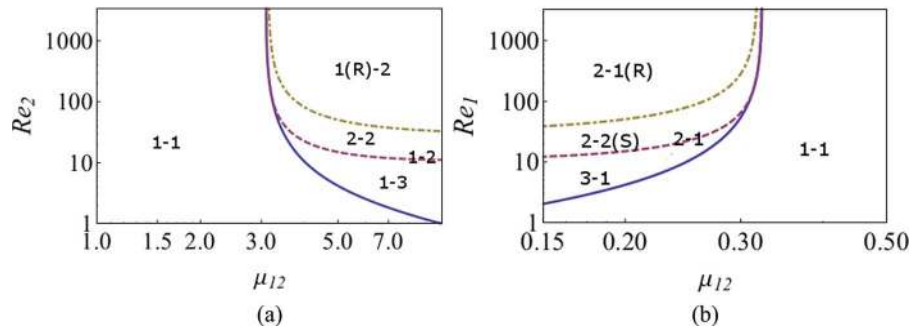


FIG. 9. Flow regime maps in (a) Re_2 - μ_{12} parameter plane for $k = -0.2$, $Re_1 = 1$, and $\lambda = 1$ (b) Re_1 - μ_{12} parameter plane for $k = 0.2$, $Re_2 = 1$, and $\lambda = 1$.

caused by the effect of parameters on the following two factors: (i) the location of the maximum base axial velocity ($w_{i,0}$) and (ii) the inter-fluid competition.

1. Case of similar fluid properties and volume fractions

When the fluids have similar properties and volume fractions ($\mu_{12} \sim 1$, $Re_1 \sim Re_2$, $k \sim 0$), the maximum of the base axial velocity is located near the interface ($y \sim k \sim 0$). Thus we have a 1–1 configuration (Type 1), with a principle vortex in each fluid. This flow field is similar, in appearance, to the single phase case (Fig. 2). In the following discussion, we treat this situation as the base case, and examine the flow pattern transitions which occur on varying each of the parameters.

2. Influence of the viscosity ratio

When the viscosity ratio is near unity, then the maximum of the axial velocity is located near the center of the channel. If the interface is located at the center, as well (equal volume fractions), then we have the 1–1 configuration. However, if the fluids have significantly different viscosities, then the less viscous fluid flows faster, and the maximum of $w_{i,0}$ is located within the bulk of the less viscous fluid. Therefore, when the viscosity ratio is increased above unity (fluid 2 is less viscous) the maximum shifts into the fluid 2; this results in the formation of spilt vortices in fluid 2. Thus we have a transition from the 1–1 pattern to the 1–3 pattern (Fig. 9(a)). On the other hand, if the viscosity ratio is decreased, below unity, then the maximum of $w_{i,0}$ shifts into fluid 1, and we have a transition from the 1–1 to 3–1 configuration (Fig. 9(b)).

Apart from its influence on the location of the maximum base axial velocity, the viscosity ratio plays an important and subtle role in the inter-fluid interaction. At viscosity ratios near unity, the more viscous fluid controls the flow at the interface and forces the less viscous fluid to locally reverse its flow. Thus, the 1–3 pattern is found at μ_{12} greater than unity (cf. Fig. 9(a)); here the more viscous fluid 1 induces a sandwich vortex in fluid 2 (less viscous). Analogously, at viscosity ratios below unity we have the 3–1 pattern; wherein, fluid 1 (less viscous) contains a sandwich vortex (cf. Fig. 9(b)). However, this is only one aspect of the dual role played by viscosity in the inter-fluid competition. The second effect dominates at *extreme viscosity ratios*, large or small, when the Reynolds number of the less viscous fluid is greater. The less viscous fluid has a much higher axial velocity and consequently experiences stronger centrifugal forces, compared to the more viscous fluid. Thus, at very high viscosity ratios, the less viscous second fluid begins to dominate the flow. In the case of Fig. 9(a), increasing μ_{12} causes the sandwich vortex to shift from fluid 2 to fluid 1 (1–3 to 2–2 transition). The sandwich vortex in fluid 1 then grows in size, as the viscosity of fluid 1 is increased further, until it occupies the entire fluid and becomes a reversed vortex (2–2 to 1(R)-2 transition). Note that this requires the Reynolds number of the less viscous fluid 2 to be greater than that of fluid 1 ($Re_1 < Re_2$) – this is true at large μ_{12} , if the fluids have similar densities. The opposite series of Type 3 transitions – occur on decreasing μ_{12} below unity, with $Re_1 > Re_2$ – in Fig. 9(b); the

sandwich vortex shifts from fluid 1 to fluid 2 (3–1 to 2–2(s) transition), where it ultimately becomes a reversed vortex (2–2(s) to 3–1(R) transition).

The influence of the relative viscosities on the flow pattern is closely related to the relative Reynolds number of the fluids. Thus in Fig. 9, the full range of flow patterns cannot be observed by varying the viscosity ratio alone; rather, it requires changes in the Reynolds numbers (densities) of the fluids as well. The physical role played by the Reynolds number is discussed next.

3. Influence of the Reynolds numbers

In this analysis, the Reynolds numbers represent the strength of centrifugal forces relative to viscous forces within each fluid. The Reynolds number will be higher for the fluid of greater density and lower viscosity. Fig. 9 demonstrates the significant impact of the Reynolds numbers on the flow pattern. However, this figure also shows that differences in the Reynolds numbers are unimportant when the viscosity ratio is near unity and the volume fraction is near 0.5. In fact, Fig. 9(a) has a threshold viscosity ratio of 3.08, above which the Reynolds numbers begin to affect the flow pattern. This occurs because the Reynolds number does not affect the base flow profile and has no influence over the location of the maximum of $w_{i,0}$. Hence, split vortices cannot be formed by solely varying the Reynolds numbers of the two fluids; variation of the viscosity ratio or the interface position is necessary to cause transitions between 1–1 and 1–3 (or 3–1) patterns.

If the viscosity ratio or the interface position is such that Type 2 (or Type 3) patterns are possible, then the Reynolds numbers of the two fluids play an important role. Their relative magnitudes have a significant impact on the inter-fluid competition: the fluid with the higher Reynolds number has a tendency to control the flow near the interface, since it experiences stronger centrifugal forces. Thus in Fig. 9(a), increasing Re_2 pushes the sandwich vortex from fluid 2 into fluid 1 (1–3 to 2–2 transition). Ultimately, fluid 2 completely dominates the flow, causing fluid 1 to flow against its natural tendency with a reversed vortex (the 1(R)-2 pattern). On the other hand, in Fig. 9(b), fluid 1 controls the flow at the interface, as Re_1 is increased. The sandwich vortex shifts into fluid 2, resulting in transitions from the 3–1 pattern to the 2–2(s) pattern and ultimately to the 2–1(R) configuration.

4. Influence of the volume fraction/holdup

The volume fraction of the fluids determines the location of the interface, which in turn affects both the location of the maximum of $w_{i,0}$ and the inter-fluid competition. If the fluid viscosities are similar, then the maximum of $w_{i,0}$ will be located in the fluid of higher volume fraction. Consequently, this fluid will contain split vortices. Thus decreasing (increasing) k below (above) 0.5 promotes the formation of split vortices within fluid 2 (fluid 1). This effect is illustrated by Fig. 10, which depicts the flow regime map for $k = -0.35$ and $Re_1 = 1$. In comparison with Fig. 9(a) ($k = -0.2$ and $Re_1 = 1$), the 1–1 to 1–2 transition occurs at lower μ_{12} and Re_2 ; the threshold viscosity ratio for the formation of split vortices in fluid 2 is also smaller.

Apart from influencing the formation of split vortices, the volume fraction also affects the position of the sandwich vortex. As the volume fraction of a fluid increases, its flow field must approach the single phase case. Thus sandwich vortices must shift into the fluid of lower volume fraction.

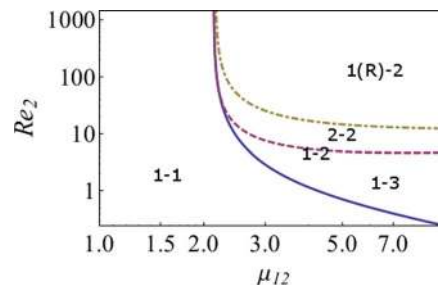


FIG. 10. Flow regime map in the $Re_2 - \mu_{12}$ parameter plane for $k = -0.35$, $Re_1 = 1$, and $\lambda = 1$.

Physically, the fluid with lower volume fraction is confined between the wall and the interface, which restricts its flow. Thus, it is dominated by the fluid with a larger volume fraction. Hence, the transition to 2–2(s) and 1(R)–2 patterns occur at lower μ_{12} and Re_2 in Fig. 10 ($k = -0.35$), compared to Fig. 9(a) ($k = -0.2$).

C. Selection of a desired flow pattern

For a specific pair of fluids, a range of flow patterns will be observed by varying the operating conditions – pressure drop and the volume fraction/holdup. The volume fraction determines k (cf. Eq. (33a)) and the pressure drop (G) specifies the magnitude of the Reynolds numbers. Experimentally, it is more convenient to vary the flow rates of the two fluids, which are related to the pressure drop and holdup via Eqs. (91) and (92). Using the results of Sec. V, the flow rates can be chosen to obtain any desired circulation pattern.

VI. ASPECT RATIO AND STRENGTH OF THE CIRCULATORY FLOW

The aspect ratio (λ) is defined as the ratio of the width of the channel to its height. The results presented thus far correspond to a square channel ($\lambda = 1$). In rectangular channels ($\lambda \neq 1$), we find the same basic cross flow configurations presented in Sec. IV; although, their exact location in parameter space differs. Flow regime maps, such as Figs. 9 and 10, can be constructed (based on the methodology presented in Sec V), to obtain more detailed information, for any specific aspect ratio.

Changing the aspect ratio has a more significant effect on the strength of the circulatory flow (the magnitude of $u_{i,1}$ and $v_{i,1}$) than on the flow pattern. In this section, we analyze the dependence of the strength of the cross-flow on the aspect ratio. To quantify the strength of the circulatory flow, we define an intensity parameter for each fluid (I_i),

$$I_1 = \left(\int_{-1}^1 \int_{-1}^k (u_{1,1}^2 + v_{1,1}^2) dy dx \right)^{1/2}, \quad (99a)$$

$$I_2 = \left(\int_{-1}^1 \int_k^1 (u_{2,1}^2 + v_{2,1}^2) dy dx \right)^{1/2}. \quad (99b)$$

We now compare the intensities of the cross-flow (I_i) in channels of different aspect ratios. To make a fair comparison, the cross sectional area of the channel is kept constant at a value of $4a^2$. Thus, a channel of aspect ratio λ has a width of $2a\sqrt{\lambda}$ and a height of $2a/\sqrt{\lambda}$. If instead one kept the width of the channel constant, then the cross-sectional area for flow ($4ab = 4a^2/\lambda$) will decrease as the aspect ratio is increased. Since the pressure drop is the same in all cases, the larger aspect ratio channels will have a much smaller axial flow; this in turn will result in a small intensity of circulation. To eliminate this bias, we keep the cross-sectional area constant and change both the width and height to obtain channels of different aspect ratios.

Another subtlety, related to the Reynolds numbers and characteristic velocity scales, arises while comparing channels of different aspect ratios. Since the width of each channel is different, its Reynolds numbers and velocity scales will differ; these will be equal to $\lambda^{3/2}Re_i$, and $\lambda V_{c,i}$, where Re_i and $V_{c,i}$ are the Reynolds numbers and velocity scales for a square channel. While comparing the values of the intensity factors, we take $V_{c,i}$ as the common scale. Thus the intensity factor for flow in a curved channel, of aspect ratio λ and cross sectional area $4a^2$, that is driven by a pressure drop of $-GR$ is

$$\bar{I}_1 = \lambda \left(\int_{-1}^1 \int_{-1}^k (u_{1,1}^2 + v_{1,1}^2) dy dx \right)^{1/2}, \quad (100a)$$

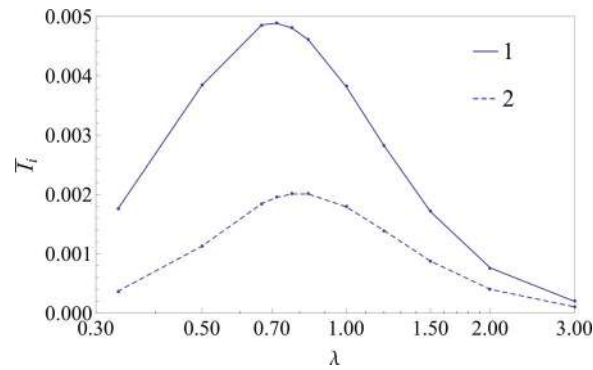


FIG. 11. Dependence of the strength/intensity of the circulatory flow on the aspect ratio. The system parameters are: $\mu_{12} = 1$, $Re_1 = 5$, $Re_2 = 1$, $k = 0$.

$$\bar{I}_2 = \lambda \left(\int_{-1}^1 \int_k^1 (u_{2,1}^2 + v_{2,1}^2) dy dx \right)^{1/2}. \quad (100b)$$

The values of these intensity factors (\bar{I}_i) are plotted for a range of aspect ratios in Fig. 11, for $\mu_{12} = 1$, $Re_1 = 5$, $Re_2 = 1$, $k = 0$. Here, we observe a considerable variation with the aspect ratio; importantly, each curve has a maximum value which corresponds to the aspect ratio that maximizes the circulation strength within that fluid. In general, the maximum of each curve will be different. Thus, one must choose between the two fluids when designing channels for an application, since the strength of the circulatory flow can be maximized in only one of them at a time. Alternatively, an intermediate aspect ratio may be more favourable in terms of increasing the overall strength of the circulatory flow. These decisions depend on the specifics of the application; calculations like those presented here will aid in designing a curved channel that provides the maximum benefit.

VII. INTERFACE DEFORMATION

A. General characteristics of the deformed interface

The secondary cross-flow ($\varepsilon u_{i,1}$ and $\varepsilon v_{i,1}$) exerts normal stresses at the interface, causing it to deform. Surface tension, on the other hand, resists this deformation. Thus, the shape of the interface is determined by a balance between these competing forces, as expressed in the normal stress condition (14). The right hand side of (14) accounts for the restoring action of surface tension, while the left hand side represents the stresses exerted by the two fluids. These stresses are composed of two parts: the pressure exerted on the interface and the viscous stress due to the normal component of velocity ($v_{i,1}$).

Figure 12 depicts the pressure distribution and the deformed interface shape, for the case of $\mu_{12} = 2$, $Re_1 = 20$, $Re_2 = 1$, $k = 0.2$, $Ca = 10$, $\varepsilon = 0.1$. The pressure is seen to increase from the inner wall ($x = -1$) to the outer wall ($x = +1$) of the channel, in both fluids (Fig. 12(a)). However, the magnitude of the pressure differs significantly in the two fluids, as shown in Fig. 12(b). At the outer wall the pressure is higher in fluid 1 than in fluid 2; whereas, at the inner wall it is lower in fluid 1. Thus the interface is pushed upward into fluid 2 at the outer wall, while at the inner wall the interface is pushed downward (Fig. 12(c)). This anti-symmetric shape is a general feature of the interface; it is a result of the anti-symmetry of the pressure distribution and the $v_{i,1}$ field.

In Sec. V, we showed that the inter-fluid interaction, at the interface, is a key factor in setting up a variety of flow patterns. Similarly, this interaction plays an important role in determining the shape of the deformed interface. In the case of the 1–2 and 2–1 flow patterns, the vertical component of velocity ($v_{i,1}$) is in the same direction at $y = k$ (the position of the interface at $O(\varepsilon^0)$). Also, the pressure decreases in opposite directions along $y = k$, since $u_{i,1}$ is in opposite directions along the

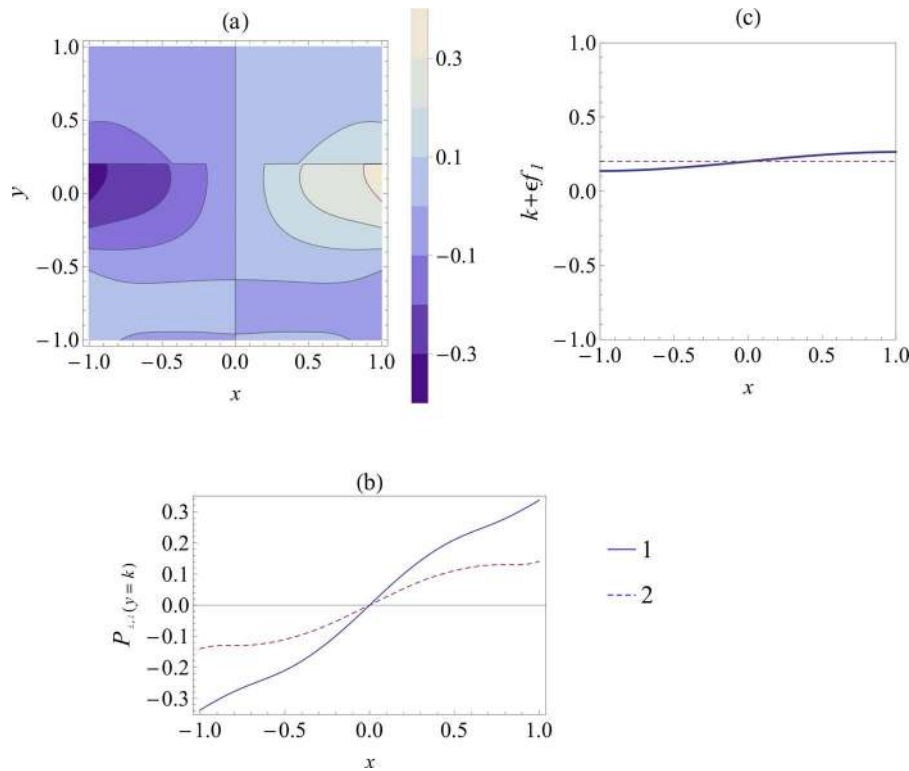


FIG. 12. (a) Pressure distribution across the cross section of the channel. (b) Variation in the pressure across the width of the channel at $y = k$, i.e., $P_{i,1}(x, k)$. Here the solid and dashed lines represent the pressures in fluid 1 and fluid 2, respectively. (c) The interface at $O(\epsilon^1)$ (solid line) along with the interface in a straight channel (dashed line). The values of the system parameters are: $\mu_{12} = 2$, $Re_1 = 20$, $Re_2 = 1$, $k = 0.2$, $Ca = 10$, $\epsilon = 0.1$.

interface. As a result, the normal stresses, exerted by the two fluids, reinforce each other to deform the interface. However, in all the other flow patterns, which account for almost all parameter values, $v_{i,1}$ is in opposite directions at $y = k$. The pressure also decreases, along the interface, in the same direction. This is the case in Fig. 12. In these situations, the stresses exerted by the two fluids counteract each other. The fluids attempt to push/pull the interface in opposite directions. In spite of this, there is a net normal stress that ultimately deforms the interface. This is because the cross flow in the two fluids are not identical. Thus one of the fluids overcomes the other and controls the shape of the interface.

In the case of Fig. 12, fluid 1 controls the shape of the interface, due to the stronger pressure gradients within it. For the opposite set of parameter values – $\mu_{12} = 1/2$, $Re_1 = 1$, $Re_2 = 20$, $k = -0.2$ – the situation will reverse and fluid 2 will exert a stronger normal stress; the interface will then deform upward at $x = -1$ and downward at $x = 1$. It is possible for the pressures within the two fluids to be similar – at appropriate parameter values – in which case, the viscous normal stress due to $v_{i,1}$ will play a prominent role. Thus the interface can deform in either direction, depending on the parameters; further, the extent of deformation will also depend on the parameter values. We study the effect of each parameter in Subsection VII C.

B. Possibility for a flat horizontal interface: An exceptional case

Due to the opposing nature of the normal stresses, exerted by the two fluids at the interface, it is possible for the interface to be flat and horizontal even at finite Ca . These exceptional situations will occur when the forces exerted by the fluids on the interface exactly balance one another.

A condition on the parameters, for this special case, can be derived by setting $f_1(x) = 0$ in (68). The resulting equation has the form $Ca \times \Phi(\mu_{12}, Re_1, Re_2, k) = 0$. For $Ca \neq 0$, this equation specifies a three dimensional manifold in a four dimensional parameter space. If the parameter values lie on

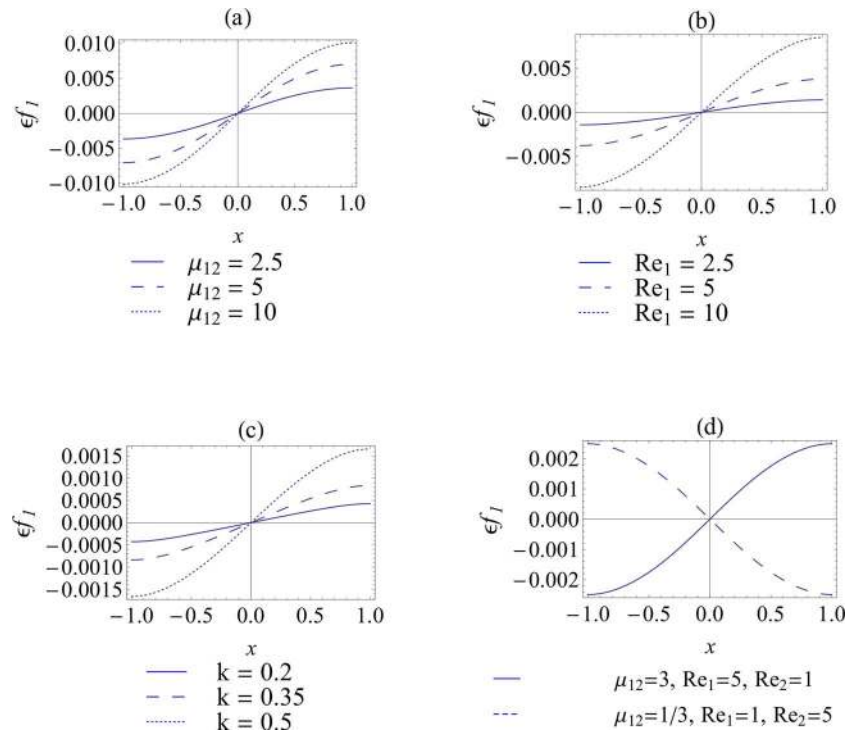


FIG. 13. Effect of varying different parameters on the deformation of the interface. (a) Effect of increasing the viscosity of fluid 1; other parameters are kept constant at $Re_1 = 1$, $Re_2 = 1$, $k = 0$. (b) Effect of increasing the Reynolds number of fluid 1; $\mu_{12} = 1$, $Re_2 = 1$, $k = 0$. (c) Effect of increasing the volume fraction of fluid 1; $\mu_{12} = 1$, $Re_1 = 1$, $Re_2 = 1$. (d) Two opposite interface shapes, obtained when fluid 1 controls the interface (solid line) and when fluid 2 controls the interface (dashed line).

this manifold, then the interface will be flat. A trivial example is the case of equal fluid properties and volume fractions: $\mu_{12} = 1$, $Re_1 = Re_2$, $k = 0$. The deformation of the interface will be smaller, the closer the parameter values are to this manifold. However, the parameters will not lie exactly on this manifold in a practical two-phase flow; thus, in general, the fully developed interface in a curved channel will be deformed.

C. Effect of parameter variations

Now we investigate the effect of varying the system parameters on the shape of the interface. We consider the case of $\mu_{12} = 1$, $Re_1 = Re_2$, $k = 0$, in which the interface remains flat, as the base case. Then the value of each parameter is varied sequentially to study its effect on the shape of the interface. In Fig. 13(a), we plot the modification to the interface shape at $O(\varepsilon^1)$ for increasingly large viscosities of fluid 1. In Fig. 13(b), three cases of increasing Re_1 are depicted, while in Fig. 13(c) we consider the case of increasing holdup (volume fraction) of fluid 1. In all these figures, the interface deformation is seen to increase with the difference between the properties of the two fluids and their volume fractions; In fact the deformation increases as the parameters are located further away from the manifold of special cases (Sec. VII B). The further these parameters are from the manifold, the more unequal are the normal stresses at the interface and the greater is the net force exerted to deform it. In Figs. 13(a)–13(c), the interface shape is controlled by fluid 1 due to stronger pressure gradients. The opposite situation is depicted in Fig. 13(d), where the fluid properties are flipped (dashed line), to allow fluid 2 to control the interface.

The effect of the capillary number can be anticipated from Eq. (68) for $f_1(x)$: the interface deformation is proportional to Ca . At low Ca , surface tension dominates and reduces the deformation of the interface; ultimately, in the limit of $Ca = 0$, the interface is flat. Ca is defined in terms of

the pressure gradient as Ga^2/γ . Thus even for moderate values of the surface tension, Ca will be low if the channel dimension (a) is small. A small channel width also ensures a small value of the curvature ratio (ε). Thus, the interface deformation in curved *microchannels* will be quite small, and the results of this work will be directly applicable.

VIII. NUMERICAL SIMULATIONS

In this section, we identify the range of Reynolds numbers and curvature ratios for which the first order perturbation solution is accurate. Towards this end, we carry out numerical simulations of the nonlinear governing equations (1)–(4) and compare the results with the perturbation solution. Here, we only consider the case of a flat vertical interface, which is a good approximation at small Capillary numbers (cf. Sec. VII).

We have developed a numerical code to solve the fully developed, nonlinear, 3D two-phase flow, in a curved channel (Eqs. (1)–(4)). The solution is obtained by iteratively solving a sequence of nonlinear, 2D two-phase flows. The numerical scheme begins with an initial guess for the velocity field. Treating the axial velocity as a known quantity, the continuity equation (1) and the momentum equations in the x and y directions (2–3) are solved to determine the 2D circulatory flow (u_i and v_i). Next, the axial velocity (w_i) is updated, by substituting the calculated values of u_i and v_i into the axial momentum equation (4) and solving for w_i . The updated w_i is, in turn, used to correct the circulatory flow. This procedure is repeated, iteratively, until the velocity fields converge. The 2D flow problem at each iteration is solved using the vorticity-stream function formulation, with a finite difference based discretization. A 160×100 (x - y) grid is required for a grid independent solution, at the Reynolds numbers investigated here (up to 400). For quicker convergence, we used the perturbation solution as the initial guess for simulations at low values of Re and ε , while continuation was used for higher values of these parameters.

Guided by the flow regime maps in Sec. V A, we carried out simulations for different parameter values, to obtain all the circulatory flow patterns. The results of the nonlinear simulations are compared with the perturbation calculation in Fig. 14, for the flow regimes studied previously in

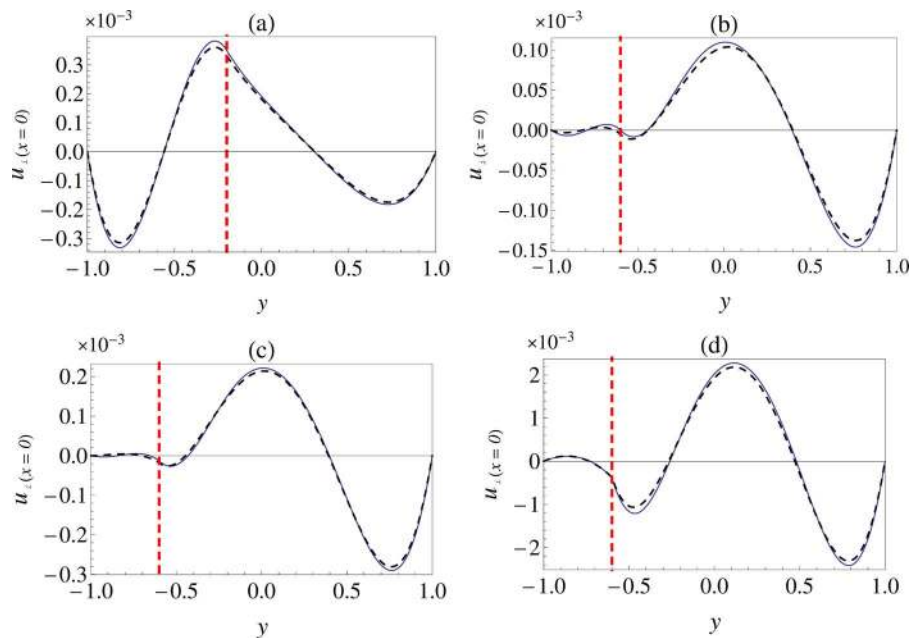


FIG. 14. Comparison of the perturbation solution with numerical simulations for different flow patterns – plots of u_i , at $x = 0$, along the vertical direction. The dashed line is the perturbation solution and the solid line is the numerical solution. (a) $Re_1 = 1$, $Re_2 = 5$, $\mu_{12} = 1$, $k = -0.2$; (b) $Re_1 = 1$, $Re_2 = 1$, $\mu_{12} = 1.2$, $k = -0.6$; (c) $Re_1 = 1$, $Re_2 = 2$, $\mu_{12} = 1.2$, $k = -0.6$; (d) $Re_1 = 1$, $Re_2 = 10$, $\mu_{12} = 3$, $k = -0.6$. In all cases, $\lambda = 1$, $\varepsilon = 0.1$.

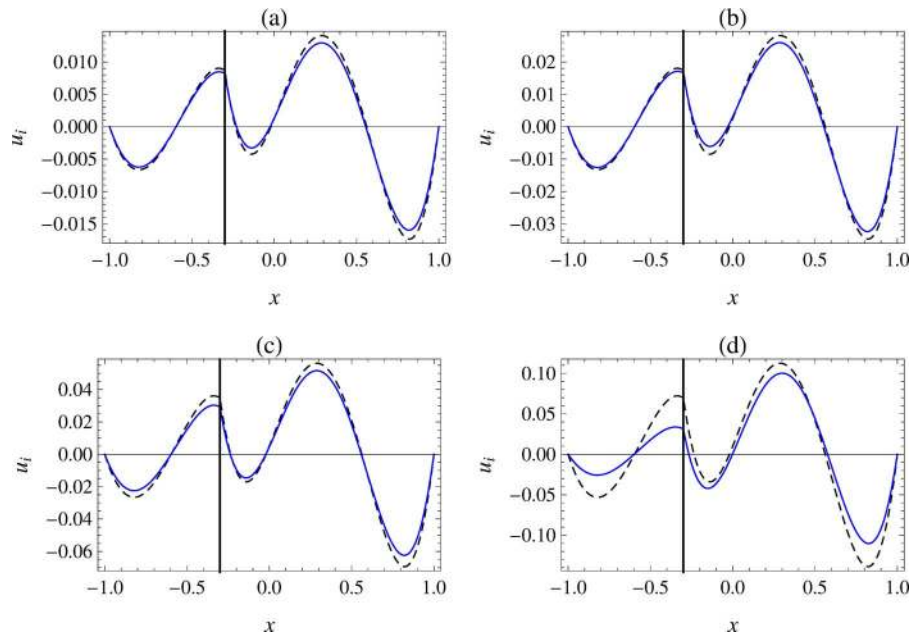


FIG. 15. Comparison of the perturbation solution with numerical simulations for increasing Re - plots of u_i , at $x = 0$, along the vertical direction. The dashed line is the perturbation solution and the solid line is the numerical solution. $\mu_{12} = 10$, $\lambda = 1$, $k = -0.3$ (a) $Re_1 = 50$, $Re_2 = 50$; (b) $Re_1 = 100$, $Re_2 = 100$; (c) $Re_1 = 200$, $Re_2 = 200$; (d) $Re_1 = 400$, $Re_2 = 400$.

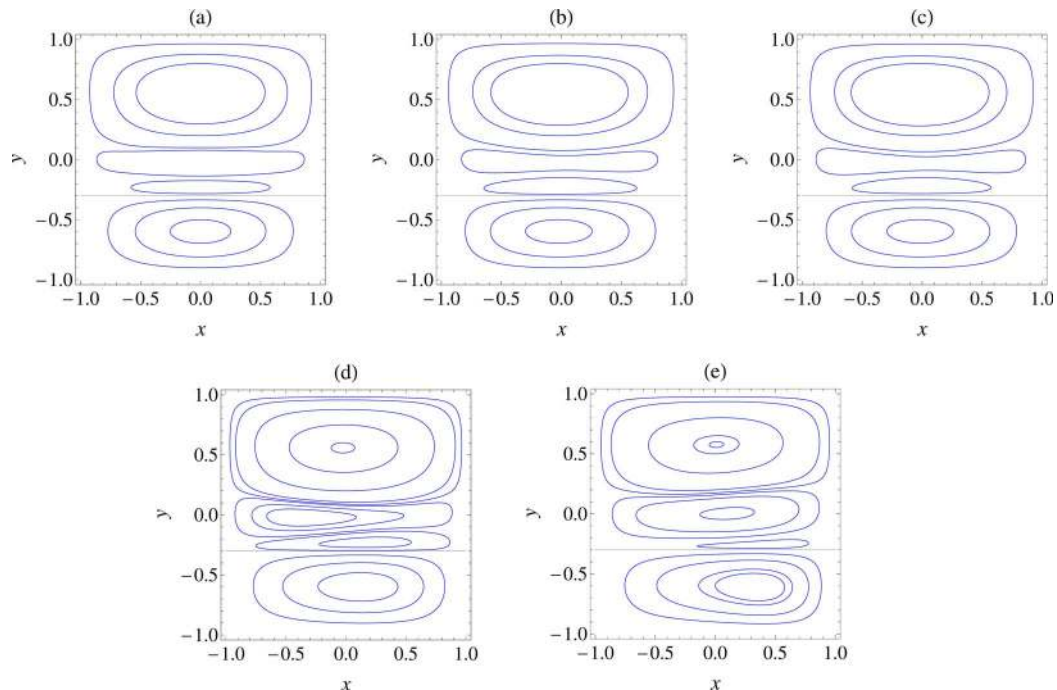


FIG. 16. Circulatory flow patterns for the 1–3 configuration at various values of the Reynolds numbers. (a) The prediction of the perturbation solution – this vortex pattern is independent of Re_1 and Re_2 . The figures (b)–(e) depict the numerical calculations: (b) $Re_1 = 50$, $Re_2 = 50$; (c) $Re_1 = 100$, $Re_2 = 100$; (d) $Re_1 = 200$, $Re_2 = 200$; (e) $Re_1 = 400$, $Re_2 = 400$. The other parameter values are $\mu_{12} = 10$, $\lambda = 1$, $k = -0.3$.

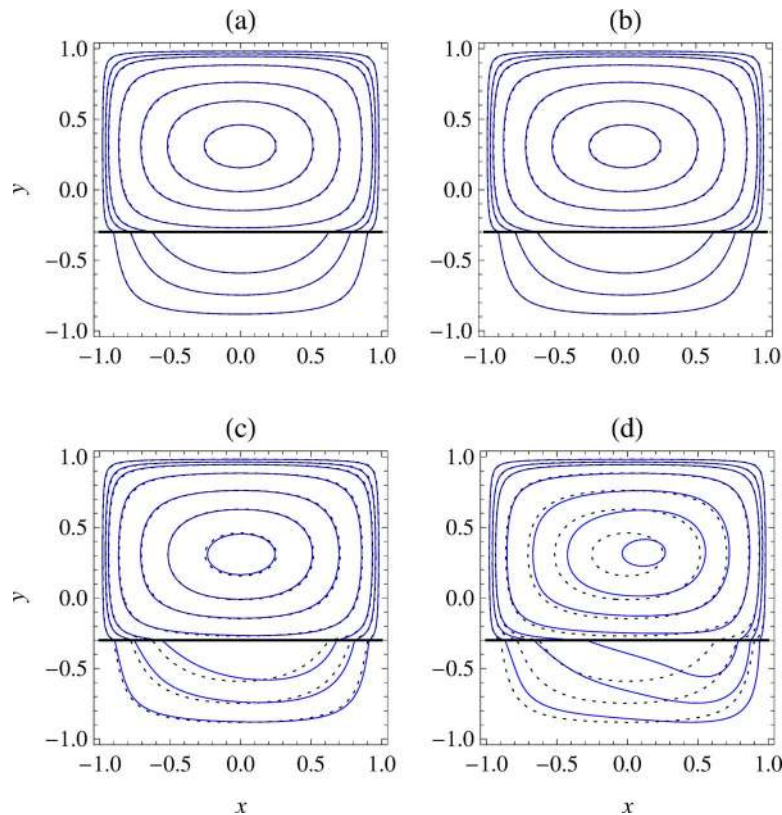


FIG. 17. Modification of the axial velocity contours in a curved channel. The dashed line contours correspond to the flow in a straight channel, while the solid line contours correspond to flow through the curved channel, as computed by numerical simulations. The contours in both cases are plotted for the same set of axial velocity values. (a) $Re_1 = 50$, $Re_2 = 50$; (b) $Re_1 = 100$, $Re_2 = 100$; (c) $Re_1 = 200$, $Re_2 = 200$; (d) $Re_1 = 400$, $Re_2 = 400$. Other parameter values: $\mu_{12} = 10$, $\lambda = 1$, $k = -0.3$.

Figs. 3 and 5–7 (Type 1 and Type 2 patterns, with the exception of the 3–1 pattern; the latter is studied in detail in the figures to follow). We find very good agreement in all cases. The small differences between the perturbation and numerical calculations in Fig. 14 are mainly due to the simplification made in the calculation of the stream function ($\psi_{i,1}$) in Sec. III B, in which we used only the first term of $w_{i,0}$ (cf. Eqs. (34) in Eqs. (49)).

Next, we study the effect of increasing the Reynolds number on the 1–3 flow configuration (cf. Fig. 4). The results of the numerical simulations, computed for Re_1 and Re_2 from 50 to 400, are compared with the perturbation solution in Figs. 15 and 16. Line plots of u_i , at $x = 0$, are compared in Fig. 15. The streamlines of the circulatory flow are presented in Fig. 16. We observe that the perturbation solution remains quite accurate up to $Re = 100$, but shows significant deviations from the numerical calculations for $Re = 200$ and above.

The first order perturbation solution does not account for the effect of increasing Reynolds numbers on the circulatory flow pattern. The streamlines of the perturbation solution (Fig. 16(a)) are independent of Re and ε ; only the magnitude of the cross-flow changes. On the other hand, the numerical simulations show significant changes in the vortex pattern at Reynolds numbers of 200 and 400 in Figs. 16(d) and 16(e). The vortices shift off-center and move towards the outer half of the channel, as the Reynolds number is increased.

The differences between the predictions of the perturbation solution and the numerical calculations at high Re are directly related to the modification of the axial velocity profile, caused by the circulatory flow. Fig. 17 depicts the contours of the axial velocity in a curved channel, along with the contours for a straight channel. The circulatory flow causes the contours to shift outwards, at higher Re . The *first order* perturbation solution is based on the axial velocity in a straight channel. Since, at

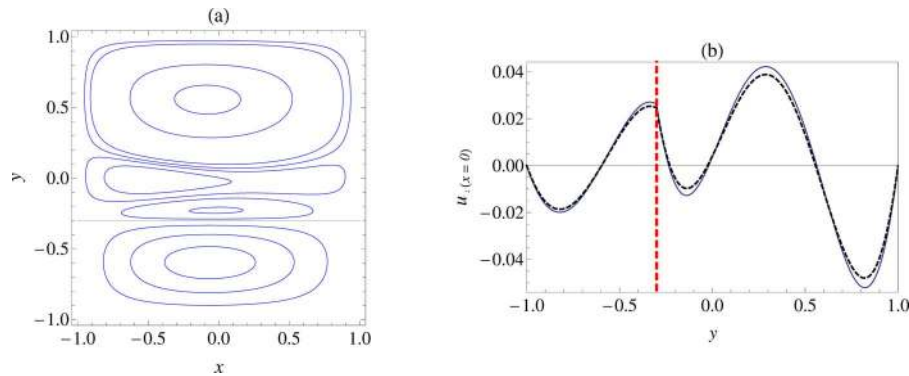


FIG. 18. Comparison of the perturbation solution with numerical simulations for a relatively high curvature ratio of $\varepsilon = 0.3$. (a) Streamlines of the cross flow. The streamlines predicted by the perturbation solution are shown in Fig. 16(a). (b) Plot of u_i , at $x = 0$. The dashed line is the perturbation solution and the solid line is the numerical solution. Parameter values: $Re_1 = 50$, $Re_2 = 50$, $\mu_{12} = 10$, $\lambda = 1$, $k = -0.3$, and $\varepsilon = 0.3$.

Re beyond 100, the circulations significantly modify the axial velocity (cf. Fig. 17), the perturbation solution fails to describe the flow accurately. To account for the modified axial velocity, one must extend the perturbation calculation to $O(\varepsilon^2)$ at least.

The numerical simulations and the perturbation solution show deviations for relatively high values of the curvature ratio, as well. An example is depicted in Fig. 18, for the 1–3 configuration, for $\varepsilon = 0.3$ and $Re_1 = Re_2 = 50$. Comparing the streamline plots in Fig. 18(a) with Fig. 16(a), we see qualitative differences in the vortex patterns. It should be noted that the perturbation calculation is more accurate for the same curvature ratio, if the Reynolds numbers are smaller.

The numerical results in this section provide an indication of the upper limit on the Reynolds numbers and curvature ratios, below which the perturbation solution is accurate. This limit is sufficiently high for the solution to be applied to practical stratified micro-flows.¹⁶

IX. CONCLUDING REMARKS

In this paper, the low Reynolds number flow of two vertically stratified fluids through a curved channel has been analyzed. We have derived an asymptotic solution, for the limit of a small curvature ratio, by applying the domain perturbation method. The solution revealed a variety of circulatory flow patterns, when analyzed across the parameter space. Nine different flow patterns have been identified and categorized based on the number and location of the secondary vortices. Two key factors determining the flow pattern are: (i) the vertical location of the maximum axial velocity, (ii) the inter-fluid competition at the interface. The first dictates the formation and location of split vortices; the second determines the location of the sandwich vortex. By studying how the parameters (Reynolds numbers, viscosity ratio, and volume fraction) influence these two pattern-generating mechanisms, one can anticipate the effect of each parameter on the cross-flow. This qualitative understanding supplements the quantitative flow regime maps presented here. These maps can be easily constructed using the analytical solution and a computationally inexpensive algorithm; this algorithm is based on special conditions that must be satisfied by the velocity field at the boundary between different flow regimes. Using these maps, one can identify the operating conditions (pressure drop and volume fraction – or the two flow rates) corresponding to a desired flow pattern.

Targeted numerical simulations confirmed the accuracy of the perturbation solution for small, but finite, values of the Reynolds numbers (up to 100) and curvature ratios (up to 0.2). Thus, the perturbation solution and the results given in this paper, along with the inferences drawn from them, may be applied with confidence to stratified micro-flows. These flows are encountered in solvent extraction^{16–18} and phase transfer catalysis.¹⁹ Carrying out these applications in curved channels will enhance intra-fluid mixing and increase the device efficiency.^{26,9} A particularly significant result in this regard is the existence of optimum aspect ratios, which maximize the strength of the cross-flow

in each fluid. Choosing these aspect ratios will maximize the benefits of using curved microchannels as inter-fluid mass transport devices.

An important issue in two-phase flows is the shape of the interface, which is unknown *a priori*. Applying the domain perturbation method, we have approximated the location of the interface to $O(\varepsilon^1)$; the results indicate that, while the interface is flat and horizontal in a straight channel, it will *almost always* deform in a curved channel (in case of finite Capillary numbers). This result is non-obvious because the centrifugal force is horizontally directed, with no component perpendicular to a horizontal surface. The principle cause of the deformation is the *indirect* action of the centrifugal force, via the cross-flow which exerts a net normal stress on the interface. However, this fact alone is insufficient to guarantee a deformed interface, since the stresses exerted by the two fluids are oppositely directed, in most cases, and counter-act each other. The deformation becomes inevitable because the flow in each fluid is almost always non-identical – with different pressure and velocity fields. Thus the associated normal stresses are unequal and lead to a resultant normal force which deforms the interface. Exceptional cases do exist, but correspond to a three dimensional manifold of parameter values embedded in a four dimensional parameter space- a subset which in practice will never be exactly realized. Therefore, in a practical two-phase flow, the interface will most likely deform (unless the Capillary number is very low).

The interface attains an anti-symmetric shape about the vertical mid-plane of the cross section. It deflects upward at one lateral wall and downward at the other, while retaining the same position at the center. The direction of deflection is dictated by the fluid that exerts the greater normal stress. Thus, in addition to the extent of deformation, the direction of deflection also depends on the parameter values. The capillary number (Ca), which is inversely related to the strength of surface tension forces, is a key parameter; the deformation at $O(\varepsilon^1)$ is directly proportional to it.

Before concluding, some comments on the stability of stratified flow in curved channels are in order. The interface is susceptible to a viscosity induced mode and a Rayleigh-Taylor mode; these modes have been studied in the context of stratified flows between flat plates. However, both these modes are stabilized by surface tension at low capillary numbers. Stable interfaces in stratified flows have been reported in straight and curved microchannels.^{16,27,17,18} The flow can also become unstable due to the action of centrifugal forces within the bulk of the fluid. In single phase flow, the pair of Dean vortices becomes unstable at *high Reynolds numbers* and bifurcates to a four vortex solution.⁴ Therefore, on the basis of the current literature and available experiments, we expect the flow to be *stable at low values* of the Reynolds number, the curvature ratio and the capillary number – the same conditions under which the asymptotic solution is applicable. Specific stability results for stratified flow in curved channels are currently unavailable. This study provides the flow field corresponding to the base steady state; this solution is the starting point for a linear stability analysis.

In conclusion, we highlight the important characteristics of this two-phase problem. They are: (i) a source of vorticity (centrifugal forces) at low Reynolds numbers, (ii) inter-fluid interaction at an interface and (iii) several independent dimensionless parameters. These characteristics result in a rich variety of flow patterns, even in the regime of weak nonlinearity (low Reynolds numbers and curvature ratios). The asymptotic perturbation analysis has enabled us to study the system across parameter space in detail, providing insight into the behavior of the system at low Reynolds numbers. This knowledge provides a basis for future experimental studies, to visualize the circulation patterns and harness the potential of these flows for microfluidic applications.

APPENDIX: SOLUTION OF THE STREAM FUNCTION EQUATIONS

Equations (49) are recast into a linear operator form

$$(L_x + L_y)^2 \psi_i = -\lambda \text{Re}_i \frac{dw_{i,o}^2}{dy}, \quad (\text{A1})$$

where L_x and L_y are linear operators, defined as $L_x = -\frac{\partial^2}{\partial x^2}$ and $L_y = -\lambda^2 \frac{\partial^2}{\partial y^2}$.

The operators L_x and L_y , along with the boundary conditions in x and y , define three eigen value problems

$$L_x \phi_x = \omega_n^2 \phi_x \quad \phi_x(+1) = \phi_x(-1) = 0 \quad \text{for } -1 \leq x \leq 1, \quad (\text{A2})$$

$$L_y \phi_{y,1} = \omega_{m,1}^2 \phi_{y,1} \quad \phi_{y,1}(-1) = \phi_{y,1}(k) = 0 \quad \text{for } -1 \leq y \leq k, \quad (\text{A3})$$

$$L_y \phi_{y,2} = \omega_{m,2}^2 \phi_{y,2} \quad \phi_{y,2}(k) = \phi_{y,2}(+1) = 0 \quad \text{for } k \leq y \leq 1. \quad (\text{A4})$$

L_x and L_y are self-adjoint bounded linear operators; thus, the eigen vectors of (A2) to (A3) form basis sets in the Hilbert spaces $L_2[-1, 1]$, $L_2[-1, k]$, and $L_2[k, 1]$, respectively. These basis sets are used to represent the solution. First, we compute the eigen functions as follows.

Since the forcing term in (A1) and the boundary conditions (50)–(61) are even in x , only the even eigen functions of (A2) are considered. Thus we have

$$\phi_x = \cos\left(\frac{(2n-1)\pi x}{2}\right); \quad \omega_n = \frac{(2n-1)\pi}{2} \quad \text{for } n = 1, 2, 3, \dots \quad (\text{A5})$$

Solving the other two eigen value problems in each fluid, we obtain

$$\phi_{y,1} = \left(\frac{2}{1+k}\right)^{1/2} \sin\left(\frac{m\pi(y-k)}{1+k}\right), \quad \omega_{m,1} = \frac{m\pi\lambda}{1+k} \quad \text{for } m = 1, 2, 3, \dots, \quad (\text{A6})$$

$$\phi_{y,2} = \left(\frac{2}{1-k}\right)^{1/2} \sin\left(\frac{m\pi(y-k)}{1-k}\right), \quad \omega_{m,2} = \frac{m\pi\lambda}{1-k} \quad \text{for } m = 1, 2, 3, \dots \quad (\text{A7})$$

Now, the solution to (A1) is written in terms of these eigen functions.

$$\psi_i(x, y) = \sum_{m=1}^{\infty} a_{m,i}(x) \phi_{y,i} + \sum_{n=1}^{\infty} b_n(y) \phi_x, \quad (\text{A8})$$

where the coefficients $a_{m,i}$ of $\phi_{y,i}$ are functions of x , while the coefficients b_n of ϕ_x are functions of y .

In (A8), the second sum- involving ϕ_x - satisfies the homogenous forms of Eqs. (A1) respectively, while the first sum- involving $\phi_{y,i}$ - satisfies the inhomogeneous forms. Therefore to find the coefficients $a_{m,i}$ and b_n , we substitute (A8) into the respective equations and project along the eigen functions; this results in the following set of ODEs,

$$\left(D_y^4 - \frac{2\omega_n^2}{\lambda^2} D_y^2 + \frac{\omega_n^4}{\lambda^4}\right) b_n = 0 \quad \text{where } D_y = \frac{d}{dy}, \quad (\text{A9})$$

$$\left(D_x^4 - 2\omega_{m,i}^2 D_x^2 + \omega_{m,i}^4\right) a_{m,i} = -\text{Re}_i \lambda \int \frac{d(w_{i,o}^2)}{dy} \phi_{y,i} dy \quad \text{where } D_x = \frac{d}{dx}. \quad (\text{A10})$$

On solving (A9) and (A10) for $a_{m,i}$ and b_n we obtain the general solution (62)–(65); here C_1 to C_{12} are arbitrary constants, to be determined using the boundary conditions.

Applying the Dirichlet boundary conditions is straightforward. On the other hand, applying the Neumann boundary condition results in an equation with distinct functions of x (or y). Such an equation must be satisfied at every value of x (or y). To determine the value of the constants, we project out the equation along each of the N basis functions ϕ_x (or $\phi_{y,i}$); this yields N algebraic equations.

For example, the Dirichlet condition (50) at $x = 1$ can be applied for every m ranging from 1 to N , to yield N equations

$$C_1 \cosh(\omega_{m,1}) + C_2 \sinh(\omega_{m,1}) + S_1 \left(\frac{1}{\omega_{m,1}^4} + \frac{(-1)}{(\pi^2 + \omega_{m,1}^2)^2}\right) = 0. \quad (\text{A11})$$

Equation (54) at $x = 1$ is an example of a Neumann boundary condition

$$\sum_{m=1}^{\infty} [C_1 \omega_{m,1} \sinh(\omega_{m,1}) + C_2 (\sinh(\omega_{m,1}) + \omega_{m,1} \cosh(\omega_{m,1}))] \phi_{y,1} + \sum_{n=1}^{\infty} \frac{(2n-1)\pi(-1)^{n+2}}{2} (C_3 \cosh(\frac{\omega_n y}{\lambda}) + C_4 \sinh(\frac{\omega_n y}{\lambda}) + C_5 y \cosh(\frac{\omega_n y}{\lambda}) + C_6 y \sinh(\frac{\omega_n y}{\lambda})) = 0 \quad (\text{A12})$$

(A12) contains distinct functions of y ; it must be projected along the N basis functions $\phi_{y,1}$ ($m = 1, 2, 3, \dots, N$) to obtain N equations

$$C_1 \omega_{m,1} \sinh(\omega_{m,1}) + C_2 (\sinh(\omega_{m,1}) + \omega_{m,1} \cosh(\omega_{m,1})) + \sum_{n=1}^{\infty} \frac{(2n-1)\pi(-1)^{n+2}}{2} \left(C_3 \int_{-1}^k \cosh(\frac{\omega_n y}{\lambda}) \phi_{y,1} dy + C_4 \int_{-1}^k \sinh(\frac{\omega_n y}{\lambda}) \phi_{y,1} dy + C_5 \int_{-1}^k y \cosh(\frac{\omega_n y}{\lambda}) \phi_{y,1} dy + C_6 \int_{-1}^k y \sinh(\frac{\omega_n y}{\lambda}) \phi_{y,1} dy \right) = 0. \quad (\text{A13})$$

Here, $m = 1, 2, 3, \dots, N$. These N projected equations ensure that the approximate series solution, with N basis functions, closely satisfies (A12). The error at this boundary condition is orthogonal to the first N functions of the orthonormal basis set $\phi_{y,1}$. Thus the error decreases as N is increased; taking more eigen functions in the solution not only increases the accuracy of the solution within the domain, but also at the boundary.

Continuing in a similar fashion, we obtain equations to determine all the constants. Since the solution is even in x , application of the boundary conditions at $x = 1$ automatically ensures that the conditions at $x = -1$ are satisfied. Thus we have to apply 12 boundary conditions instead of 16. Ultimately we obtain a set of $12N$ coupled linear equations for the $12N$ constants. Each time N is increased all the constants have to be re-evaluated, to obtain the refined solution.

- ¹ W. R. Dean, "XVI. Note on the motion of fluid in a curved pipe," *Philos. Mag.* **7**, 208 (1927).
- ² H. G. Cuming, "The secondary flow in curved pipes," *Aeronaut. Res. Council. Reports Memo.* **1952**, 2880.
- ³ L. S. Berger, S. A. Tablot, L. Yao, "Flow in curved pipes," *Annu. Rev. Fluid Mech.* **15**, 461 (1983).
- ⁴ K. H. Winters, "A bifurcation study of laminar flow in a curved tube of rectangular cross-section," *J. Fluid Mech.* **180**, 343 (1987).
- ⁵ J. A. C. Humphrey, A. M. K. Taylor, and J. H. Whitelaw, "Laminar flow in a square duct of strong curvature," *J. Fluid Mech.* **83**, 509 (1977).
- ⁶ S. Ghosh, G. Das, and P. K. Das, "Simulation of core annular in return bends — A comprehensive CFD study," *Chem. Eng. Res. Des.* **89**, 2244 (2011).
- ⁷ M. Muradoglu and H. A. Stone, "Motion of large bubbles in curved channels," *J. Fluid Mech.* **570**, 455 (2007).
- ⁸ V. Kumar, S. Vashisth, Y. Hoarau, and K. D. P. Nigam, "Slug flow in curved microreactors: Hydrodynamic study," *Chem. Eng. Sci.* **62**, 7494 (2007).
- ⁹ A. Y. Gelfgat, A. L. Yarin, and P. Z. Bar-Yoseph, "Dean vortices-induced enhancement of mass transfer through an interface separating two immiscible liquids Dean vortices-induced enhancement of mass transfer through an interface separating two immiscible liquids," *Phys. Fluids* **15**, 330 (2003).
- ¹⁰ J. R. Picardo and S. Pushpavanam, "Core-annular two-phase flow in a gently curved circular channel," *AIChE J.* **59**, 4871 (2013).
- ¹¹ S. Vashisth, V. Kumar, and K. D. P. Nigam, "A review on the potential applications of curved geometries in process industry," *Ind. Eng. Chem. Res.* **47**, 3291 (2008).
- ¹² T. J. Pedley, *The Fluid Mechanics of Large Blood Vessels* (Cambridge University Press, 2008).
- ¹³ D. Di Carlo, "Inertial microfluidics," *Lab Chip* **9**, 3038 (2009).
- ¹⁴ A. P. Sudarsan and V. M. Ugaz, "Multivortex micromixing," *Proc. Natl. Acad. Sci. U.S.A.* **103**, 7228 (2006).
- ¹⁵ A. Aota and T. Kitamori, "Parallel multiphase microflows: Fundamental physics, stabilization methods and applications," *Lab Chip* **9**, 2470 (2009).
- ¹⁶ P. Kuban, J. Berg, and P. Dasgupta, "Vertically stratified flows in microchannels: Computational simulations and applications to solvent extraction and ion exchange," *Anal. Chem.* **75**, 3549 (2003).
- ¹⁷ P. Znidarsic-Plazl and I. Plazl, "Steroid extraction in a microchannel system—Mathematical modelling and experiments," *Lab Chip* **7**, 883 (2007).
- ¹⁸ U. Novak, A. Pohar, I. Plazl, and P. Žnidaršič-Plazl, "Ionic liquid-based aqueous two-phase extraction within a microchannel system," *Sep. Purif. Technol.* **97**, 172 (2012).

- ¹⁹ S. Aljbour, H. Yamada, and T. Tagawa, "Sequential reaction-separation in a microchannel reactor for liquid-liquid phase transfer catalysis," *Top. Catal.* **53**, 694 (2010).
- ²⁰ M. Van Dyke, *Perturbation Methods In Fluid Mechanics* (The Parabolic Press, Stanford, CA, 1975).
- ²¹ A. B. Vir, S. R. Kulkarni, J. R. Picardo, A. Sahu, and S. Pushpavanam, "Holdup characteristics of two-phase parallel microflows," *Microfluid. Nanofluid.* **013**, 1269 (2013).
- ²² V. V. Meleshko, "Biharmonic problem in a rectangle," *Appl. Sci. Res.* **58**, 217 (1998).
- ²³ R. Cornish, "Flow in a pipe of rectangular cross-section," *Proc. R. Soc. A* **120**, 691 (1928).
- ²⁴ D. Ramkrishna and N. Amundson, *Linear Operator Methods in Chemical Engineering with Applications to Transport and Chemical Reaction Systems* (Prentice Hall, New Jersey, 1985).
- ²⁵ W. R. Dean, "LXXII The streamline motion of fluid in a curved pipe (Second Paper)," *Philos. Mag.* **7**, 673 (1928).
- ²⁶ V. Hessel, H. Löwe, and F. Schönfeld, "Micromixers—A review on passive and active mixing principles," *Chem. Eng. Sci.* **60**, 2479 (2005).
- ²⁷ X. Mao, J. R. Waldeisen, B. K. Juluri, and T. J. Huang, "Hydrodynamically tunable optofluidic cylindrical microlens," *Lab Chip* **7**, 1303 (2007).